THE DIODE ARRAY VELOCIMETER

by

Edward J. Smith

Thesis submitted to the Faculty of the

Virginia Polytechnic Institute and State University

in partial fulfillment of the requirements for the degree of

MASTER OF SCIENCE

in

Aerospace and Ocean Engineering

APPROVED:

W. J. Devenport, Chairman

R. L. Simpson

D. A. Walker

May, 1992

Blacksburg, Virginia

The Diode Array Velocimeter

by

Edward J. Smith

Committee Chairman: William J. Devenport
Aerospace and Ocean Engineering

(ABSTRACT)

A novel, point measurement, proof-of-concept laser velocimeter has been developed and tested. The diode array velocimeter (DAV) uses a single laser beam for its probe. The DAV measures velocity within a seeded, transparent medium by timing the passage of a seed particle's image across an array of PIN photodiodes. This prototype device can measure one component of mean velocity as well as one component of time-averaged turbulence intensity. The concept for the DAV is rather simple. It also has an advantage over existing laser velocimeters in that it is relatively inexpensive.

Measurements made with the prototype DAV are compared to those made by a single hot-wire anemometer in a turbulent wall bounded flow with a freestream velocity of 10 m/s. The prototype DAV was found to be accurate to within 10% of

U_e in mean velocity, and within 1.5% of U_e in turbulence intensity. The prototype DAV can measure mean velocities as great as 60 m/s. It has the potential for making measurements in highly turbulent reversing flows.

Abstract

Acknowledgements

I would like to thank my advisor Dr. Devenport for his guidance and the encouragement he has given me over the last couple of years. This project was his brain-child and I'm glad I had the opportunity to help bring it to life. I must also thank Dr. Simpson and Dr. Walker for their helpful insights and for taking the time to answer my endless barrage of questions.

There were many co-workers that offered me assistance when I needed it. Thanks to Mike Rife and Jeff Zsoldos for helping me make the hot-wire measurements, and to Alan Roach for designing the laser table and many of the associated mounts.

I also wish to thank Amy Mosby for being there for me; for keeping my head above water and my priorities straight. Without her love I might not have been able to complete this work.

This work was funded by the National Science Foundation.

Table of Contents

List of Figures ix

List of Nomenclature xiii

1.0 Introduction 1

1.1 Various Types of Velocimeters 2

1.1.1 The Hot-Wire Anemometer 2

1.1.2 The Pulsed-Wire Anemometer 3

1.1.3 Laser-Doppler Anemometry 4

1.1.4 Laser-two-Focus Anemometry 5

1.1.5 Single Beam Laser Velocimetry 6

1.1.6 Mosaic Laser Velocimetry 6

1.1.7 Particle Image and Laser Speckle Velocimetry 7

1.1.8 Particle Tracking Velocimetry 8

1.1.9 Digital Image Velocimetry 9

1.2 Diode Array Velocimeter Concept 10

1.3 Research Objectives 11

2.0 Laboratory Facilities 12

2.1 Wind Tunnel 12

2.2 Artificial Seeding 13

2.3 Laser and Table 14

2.4 Hot-Wire Equipment 15

2.5 Health Precautions 16

3.0 The Prototype DAV System 17

3.1 Description of the One-Component Prototype DAV 17

3.1.1 Sending/Receiving Optics 17

3.1.2 Detector and Amplification Circuitry 18

3.1.3 Trigger Circuitry 19

3.1.4 Digital Circuitry 21

3.1.5 Validation Circuit 23

3.1.6 Computer and Digital Interface 23

3.1.7 Example of How the Prototype DAV Processes an Optical Signal 24

3.2 Measurements Made With the Prototype DAV 25

3.3 Design Considerations 26

3.3.1 Scattered Light Power 26

3.3.2 Sending/Receiving Optics 28

3.3.2.1 Alternative Receiving Lenses 30
3.3.3 The Detector and the Current-to-Voltage Converter 33
3.3.3.1 The Prototype DAV's Dynamic Response Characteristics 35
3.3.3.2 Interfering Effects 36
3.3.3.3 Theoretical Noise Calculations 38
3.3.3.4 Other Primary Stage Amplifier Circuits Tested . 40
3.3.4 Second Stage Amplifier 41
3.3.5 Example Analog Signals 42
3.3.6 The Analog to Digital Interface 44
3.3.7 The Validation Scheme 45
3.3.8 The Digital Interface Board 47

4.0 Velocity Measurements & Discussion 48
4.1 Sources of Bias Error in Measurements Made with the DAV 48
4.1.1 Rise Time and Noise 48
4.1.2 Geometry of the Detector Array 49
4.1.3 Sources of Bias Error Inherent to the Prototype DAV Only 50
4.2 Sources of Uncertainty in the Present Velocity Measurements . . . 53
4.2.1 Prototype DAV 53

4.2.2 Hot-Wire Anemometer 54
4.3 Operation of the Prototype DAV 55
4.4 Velocity Measurements of a Rotating Disk 55
4.4.1 Mean Velocity Measurements 56
4.4.2 Turbulence Intensity Measurements 58
4.5 Velocity Measurements in a Turbulent Wall Bounded Flow 61
4.5.1 Mean Velocity Measurements 62
4.5.2 Turbulence Intensity Measurements 64

5.0 Conclusions 67

Bibliography 69

Figures 72

Vita 120

List of Figures

Figure 1 A single sensor hot-wire anemometer 73

Figure 2 A standard pulsed-wire probe (Devenport, *et al.*, 1990) 74

Figure 3 A dual-beam type laser-Doppler anemometer with receiving optics in the back-scatter mode 75

Figure 4 An L2F measurement volume geometry showing 'start' and 'stop' beams (Flugge, 1983) 76

Figure 5 (a) The 10×10 mosaic detector for mosaic laser velocimetry; different operating configurations: (b) dash mode, (c) L2F mode (Cho, 1989) 77

Figure 6 A typical setup for measuring one, two, or three velocity components with the DAV 78

Figure 7 PIN photodiode detector arrays for the DAV: (a) 1-D detector array, (b) 2-D detector array 79

Figure 8 The open circuit wind tunnel used to test the prototype DAV . 80

Figure 9 The seeder for the wind tunnel (note: drawings are not to scale) 81

Figure 10 Photograph of laser table mounted to a milling machine traverse; also shown are the laser, beam steerer, and mask attached to an optical rail 82

Figure 11 A schematic representation of the prototype DAV's circuitry with the bi-cell photodiode detector (not to scale) 83

Figure 12 The co-ordinate system 84

Figure 13 The optical layout for the prototype DAV; flow travels into the paper 85

Figure 14 The receiving lens and the detector mounted to the laser table 86

Figure 15 The bi-cell PIN photodiode used for the detector with the prototype DAV; the gap between the diodes is not to scale (Silicon Detector Corp., 1984) 87

Figure 16 The amplification circuitry for one channel of the prototype DAV 88

Figure 17 Non-inverting Schmidt trigger circuit 89

Figure 18 Pre-conditioning circuit for the trigger level voltage and the amplified signal 90

Figure 19 Digital timing circuit for prototype DAV 91

Figure 20 The validation circuit; the two halves of the circuit (separated by the BNC cables) are powered from different voltage supplies 92

Figure 21 The steps involved in processing the optical signals produced by a particle's image as it crosses over the detector array 93

Figure 22 Scattered light power vs. orientation angle for receiving lens diameters of 2.54, 5.08, and 7.62 cm; calculated by the computer program STREU (Naqwi and Durst, 1989) 95

Figure 23 Measurement volume geometry for the prototype DAV; dimensions are for $\psi = 45^{\circ}$; 3 view drawing is to scale 96

Figure 24 Amplified voltage signals generated by the prototype DAV measuring the speed of a rotating disk using the camera lens for the receiving lens 97

Figure 25 Amplified voltage signals generated by the prototype DAV measuring the speed of a rotating disk using a compound receiving lens 98

Figure 26 Amplified voltage signals generated by the prototype DAV measuring the speed of a rotating disk using a masked compound receiving lens 99

Figure 27 Frequency response of both channels of the amplification circuitry for the prototype DAV 100

Figure 28 Phase response of both channels of the amplification circuitry for the prototype DAV 101

Figure 29 Power supply noise for four different power supplies 102

Figure 30 Output prototype signal noise due to four different power supplies (same power supplies of Figure 29) 103

Figure 31 Effect of signal gain peaking on the amplification circuit's frequency response 104

Figure 32 Effect of signal gain peaking on the amplification circuit's phase response 105

Figure 33 Equivalent noise circuit for the primary stage of the prototype DAV's circuitry 106

Figure 34 Various voltage signals produced by the prototype DAV while measuring a seeded flow with a freestream velocity of 10 m/s . 107

Figure 35 Leading edge of an idealized voltage signal with peak-to-peak noise bands shown 111

Figure 36 A noisy voltage signal crossing its trigger level causes the comparator amplifier's output to switch states many times (multiple triggering) 112

Figure 37 Velocity histogram showing the error due to trigger misfires; graph contains approximately 1000 samples 113

Figure 38 Rotating disk speed measured by the prototype DAV vs. speed calculated by a semi-independent method; solid line has a slope of 1 114

Figure 39 Rotating wire's turbulence stress measured with the prototype DAV vs. wire's mean velocity; solid line shows theoretical curve 115

Figure 40 Velocity probability distributions of the prototype DAV's profile data; Y location of measurement is shown in upper left hand corner of each graph 116

Figure 41 Mean velocity data taken by the prototype DAV and a hot-wire anemometer in a turbulent wall bounded flow with a freestream velocity of 10 m/s 117

Figure 42 Turbulence intensity data taken by the prototype DAV and a hot-wire anemometer in a turbulent wall bounded flow with a freestream velocity of 10 m/s 118

Figure 43 Turbulence intensity measured by the hot-wire plotted with turbulence intensity measured by the prototype DAV after correcting for the prototype's estimated error 119

List of Nomenclature

a	constant equal to $\overline{i'^2_n}/A^2$
A	constant of proportionality
b	constant
C_d	photodiode capacitance
C_s	stray capacitance
e_n	signal noise
f_c	frequency cutoff
i_a	op-amp bias current
I_d	photodiode current
I_o	photodiode dark current
I_p	mean photon current
k	Boltzman's constant $(1.38\times10^{-23}$ J/°K)
k_r	photodiode radiant sensitivity
l_d	length of bi-cell photodiode
m	slope
M	magnification factor
P_s	scattered light power

q	electron charge $(1.6\times10^{-19}$ C)
R_d	photodiode resistance
R_f	feedback resistance
u	component velocity in the X direction
U_e	freestream velocity
V	voltage
V_t	rise of signal leading edge in volts
X,Y,Z	co-ordinate orthogonal directions

Greek Symbols

δt	time fluctuation due to circuit noise
Δf	circuit bandwidth
σ	standard deviation
τ_r	rise time of signal leading edge
ϕ	elevation angle of receiving optics
ψ	orientation angle of receiving optics

Subscripts

$( )_{p\text{-}p}$	peak-to-peak value
$( )_{ref}$	reference value

Superscripts

$( )'$	fluctuating value
$\overline{( )}$	time-averaged value

1.0 Introduction

The need for physical measurements of fluid characteristics in the engineering discipline has been around for many years. Before the design of an airplane or a sea vessel can be implemented to a working device, theoretical and/or computational predictions of that vehicle's performance must be checked by making actual measurements on a 'simulated vehicle' (scaled model). Experimental investigation of basic and complex flow regimes is necessary to acquire knowledge and new insight into the 'physics' that govern these flows.

Quite often, the researcher may only need to know the fluid velocity in a region or regions of the flow. The three dimensional velocity vector of a fluid particle, along with its density, define all six Reynold's stress components at a single point. A time history of the velocity can define the frequency and phase characteristics of the flow.

The types of flows that can only be understood with a knowledge of the instantaneous velocity field are too numerous to mention. Of major interest to the present work are low speed, single phase, transparent fluid flows (i.e., room temperature air and water). Complex flow regimes that we would like to be able to study are: unsteady, turbulent, 3-D boundary layers, flows over bluff bodies, and pressure driven separating flows. Proposed herein, is a novel laser velocimeter that has the potential

to make 3-D velocity measurements in all of the flows mentioned above, with equal or greater accuracy than the measurement systems currently available.

There are many types of velocimeters in use today. Some of which are discussed in this chapter (concentrating on non-intrusive laser devices). What follows is a brief summary on the state of the art, so to speak, in working velocimeters. It is not intended to be a bibliography of such velocimeters, but only a representative subset to acquaint the reader with the current technology.

1.1 Various Types of Velocimeters

1.1.1 The Hot-Wire Anemometer

Possibly the most widely used and accepted velocimeter is the hot-wire anemometer. A single wire probe consists of a very small diameter wire stretched between two relatively large diameter prongs (Figure 1). The principle behind its operation is simple. The sensor wire is electrically heated to a temperature above that of the fluid the wire is immersed in. As heat flows from the wire to the surrounding fluid, a constant temperature is maintained by rapidly varying the current that passes through the wire[†]. The fluctuating current has a direct relationship with the heat transfer rate. The heat lost from the wire depends on the properties of the fluid, as

[†]This description refers to a constant temperature anemometer. For information on a constant current anemometer see also Blackwelder (1981).

well as the properties of the sensing wire (Blackwelder, 1981).

For accurate measurements, the hot-wire anemometer must first be calibrated in the flow at the test conditions. Hot-wires are well suited to measure fluctuating velocities because they are operated continuously in time. When two or more wires are operated simultaneously on the same probe, all three velocity components may be measured. The main drawback of the hot-wire anemometer is its physical presence in the flow. It necessarily disturbs the velocity of the fluid it is trying to measure. Another drawback is the anemometers' insensitivity to absolute direction. A hot-wire cannot determine the sense of the flow making measurements in highly turbulent or reversing flows inaccurate and often useless.

1.1.2 The Pulsed-Wire Anemometer

To investigate flows that are characterized by stationary vortices, pockets of recirculation, etc., the velocimeter must be able to determine the absolute direction of the velocity. The pulsed-wire anemometer is a directionally sensitive derivative of the hot-wire anemometer.

Figure 2 details a standard pulsed-wire probe (Devenport, *et al.*, 1990). It consists of two sensor wires that are perpendicular to and on opposite sides of a centrally located pulsing wire. The velocity component normal to all three wires can be measured by timing the passage of a heated tracer of air from the pulsing wire to one of the sensing wires. The heat tracers are produced by applying a short duration voltage burst to

the pulsing wire.

Unlike a hot-wire anemometer, the pulsed-wire will not give a continuous time history of the velocity. Some heat tracers generated by the pulsing wire will miss the sensing wires, especially in a highly turbulent flow. This results in a data rate that is lower than that of a hot-wire anemometer. The spatial resolution of a pulsed-wire is generally less than that of a hot-wire.

1.1.3 Laser-Doppler Anemometry

The laser-Doppler anemometer (LDA) is a velocimeter that is inherently non-intrusive. A diagram of a dual-beam type LDA system is shown in Figure 3. Two intersecting beams of laser light create the measurement volume. Particles in the flow passing through the measurement volume scatter light which is collected and focused onto a photodetector. The system works on the principle of the interference fringe model (Doppler-effect). Wherever two coherent beams of light intersect there will be a field of interference fringes generated. If the wavefronts of the intersecting beams are planar, then the fringes will appear as parallel bands of light and dark.

Essential for the operation of LDA, and all laser velocimeters, is the infusion of seed particles into the flow that will approximately follow the motion of the fluid. In gas flows, these particles are normally introduced artificially. As tracer particles pass through the field of interference fringes, the intensity variations in the scattered light are detected by a photomultiplier tube which produces electrical signals whose

frequency is directly proportional to the particles' velocity (Durst, *et al.*, 1976).

Two or three velocity components may be measured simultaneously with the addition of one or two more interfering beams. If the beams are frequency shifted, the LDA becomes directionally sensitive. As with all 'particle' velocimeters, LDA does not give a continuous time history of the velocity. For many applications, however, this is not a major drawback. The main drawbacks to LDA systems are their complexity and cost.

1.1.4 Laser-two-Focus Anemometry

Laser-two-focus anemometry (L2F) is basically a non-intrusive analogue of the pulsed-wire anemometer. Two parallel beams of laser light are directed through the flow field. One beam is designated the 'start' beam and the other is the 'stop' beam. Particles that pass through the beams scatter light that is focused onto a detector. As a particle crosses a beam, a signal pulse is generated by the detector. The time lapse between the two pulses is that particle's 'time of flight' from one laser beam to the other. The velocity in the direction normal to the beams can be calculated knowing the time and the distance between the two beams (Flugge, 1983).

The major sources of error in L2F velocimetry come from the time of flight measurement itself, and defining the distance that a particle has traveled. These problems are more easily understood by addressing Figure 4 which shows an example geometry for the L2F measurement volume. The time of flight measurement suffers from ambiguity

in determining the exact time a particle intersects a beam. The finite diameters of the beam waists make it difficult to determine the distance travelled and the exact measured flow angle. L2F takes data at a rate that is significantly slower than LDA because many of the particles that pass through the 'start' beam do not intersect the 'stop' beam. Lastly, L2F will always have a larger measurement volume than LDA or any single beam velocimeter.

1.1.5 Single Beam Laser Velocimetry

Measuring the transit time of a seed particle through a single laser beam is another way to determine fluid velocity. Hirleman, Yue, *et al.* (1984) studied this technique (termed L1V) in relation to its potential for measuring turbulent quantities. They found that this velocimeter (which is purely 1-D) may be adequate for measuring mean velocities, but it is not suited for measuring velocity fluctuations. L1V does not measure a single velocity component, but rather measures the resultant magnitude of velocity in the plane perpendicular to the beam. Typical accuracy obtained with the L1V is an order of magnitude less than that achieved with LDA.

1.1.6 Mosaic Laser Velocimetry

The mosaic laser velocimeter (MLV) is an ingenious attempt at creating a 2-D velocimeter that requires only a single laser beam. As described by Boutier and Lefevre (1988), a group of optical fibers are arranged into a 10×10 mosaic (100 fibers) that

makes up the detector for the instrument (Figure 5(a)). The scattered light from particles traversing the beam is focused onto the detector where the particle images cross over the mosaic of fibers. Connected to the end of each fiber is a photomultiplier (PM) tube which generates a signal when a particle image crosses its respective fiber. The MLV was tested by Boutier and Lefevre in two different configurations: first, as a 1-D velocimeter using each of the 10 rows of fibers as an active trigger (dash mode), and secondly as a 2-D velocimeter mimicking the L2F approach with one fiber acting as the 'start' signal and a row of nine fibers acting as 'stop' signals (Figure 5(b,c)). In both cases only ten PM tubes were used.

In the dash mode, at least in concept, MLV can measure one component of velocity as accurately as the distance between the fibers can be measured. In the present case, a constant theoretical distance between the fibers was assumed. When operating in the L2F mode, there was some ambiguity in determining the flow angle.

The major drawbacks of this device are its complexity, and its cost. Ten PM tubes are a major expense, not to mention the fiber optic equipment. For the MLV to operate as a true 2-D device, many more PM tubes would have to be employed.

1.1.7 Particle Image and Laser Speckle Velocimetry

Unlike the aforementioned velocimeters, particle image velocimetry (PIV) and laser speckle velocimetry (LSV) are whole field techniques, which means that they can capture velocity information over a region of the flow. PIV and LSV are essentially

two different operating modes of the same instrument (Dudderar and Simpkins, 1987). A sheet of laser light is directed through the measurement medium. The seed particles in the flow scatter light as they pass through the beam. Photographs of the scattered light, called 'speckle grams', are taken. They contain optically encoded information about the instantaneous 2-D velocity field. The velocity information can be extracted either optically or digitally.

What separates PIV from LSV is the amount of overlapping images contained in the speckle grams. With LSV, a high concentration of seed particles is used to create many overlapping images on the viewing plane. Conversely, a low seeding concentration is used in PIV to obtain as few as possible overlapping images. These two velocimeters have many drawbacks. Only slow velocities may be measured (less than a few meters/second). Also, these devices commonly have a poor signal-to-noise ratio (SNR). This leads to significant ambiguity in the direction of the velocity vector. Creating multiple exposure speckle grams can increase the SNR, but they are impractical to use in highly turbulent or higher speed flows. Lastly, extracting the velocity information can be tedious and complex.

1.1.8 Particle Tracking Velocimetry

Particle tracking velocimetry (PTV) is another whole field technique that can measure two velocity components simultaneously. As with PIV and LSV, a sheet of laser light is directed through the flow. The illuminating beam is pulsed on and off

while the seed particles pass through it. A special camera is used to track the particle images. The seeding density in the flow must be sufficiently low so that there is a minimum of overlapping images. What shows up on the recording film is a group of blurred streaks that represent the particles' movement during the exposure. The direction and distance traveled by a particle are estimated by examining the recorded images. The time durations of the pulses are known, therefore the velocity may be calculated (Adamczyk and Rimai, 1988). This method of velocimetry is only truly valuable for mean velocity measurements as there is little turbulent information that can be extracted.

1.1.9 Digital Image Velocimetry

This is an image processing technique that has its origins in PIV and LSV. Digital image velocimetry (DIV) is a whole field velocimeter that uses a high speed video camera to record the scattered light from seed particles in the flow. A time sequence of single exposure images is recorded. These sampled images are digitized, enhanced, and linearly superimposed to create an image field. Unlike the multiple exposures of PIV and LSV, the superimposed images of DIV preserve the original signal-to-noise ratio. The velocity information is then extracted by a digital Fourier transformation which is relatively noise free when compared to optical Fourier transforms. Cho (1989) claims that it is more accurate than PIV or LSV in determining the magnitude and direction of the flow velocity.

Today, accurate, non-intrusive velocimeters that can measure mean as well as fluctuating velocity components are complicated and expensive devices. There is a need for a simpler and cheaper technique for making accurate velocity measurements.

1.2 Diode Array Velocimeter Concept

A novel optical instrument, the diode array velocimeter (DAV), is proposed for measuring velocities within transparent flow mediums. The DAV is a non-intrusive, instantaneous, point velocity measurement system. A single laser beam is directed through the measurement medium. When a seed particle passes through the beam it scatters light that is collected with a receiving lens and focused onto the detector. The detector consists of a geometrical array of photodiodes. The DAV measures the time it takes for a particle's image to pass from one diode to another. One, two, or three velocity components may be calculated from the measured time of flight between the diodes and the given distances between them.

A general layout for the DAV is shown in Figure 6. Although laser light is used as the probe in this study, a coherent light source is not a necessity. However, the properties of a laser make it easy to generate a small diameter beam with a large light intensity. Flow traveling in the direction of the arrows passes through the measurement volume (the laser beam). The solid particles in the flow scatter light in all directions. The receiving lens(es), here positioned in the forward scatter mode,

collects a portion of this light and focuses it onto the detector array(s). The possibility exists for one, two, or three simultaneous velocity component measurements. Figure 7(a) shows an example of a one component detector, and Figure 7(b) gives an example of a detector suitable for two or three velocity component measurements.

1.3 Research Objectives

The immediate goal of this research was to develop a prototype, proof-of-concept device that could measure one component of mean velocity and a single time-averaged turbulence intensity. The prototype DAV should be simple in its design and relatively inexpensive (two orders of magnitude less than a comparable LDA system). Henceforth, all discussion pertaining to the DAV concept in general will be addressed in the text as referring to the 'DAV', and all discussion pertaining to the prototype DAV will be addressed as referring to the 'prototype DAV' or just simply the 'prototype'.

The next chapter briefly describes the available laboratory facilities that were used for this work. **Chapter 3** gives a detailed discussion on all aspects concerning the prototype DAV's design and development. **Chapter 4** presents the velocity measurements made with the prototype DAV and compares them to those made by a hot-wire anemometer. **Chapter 5** presents the conclusions.

2.0 Laboratory Facilities

2.1 Wind Tunnel

Flow testing of the prototype DAV was done in the boundary layer type open circuit wind tunnel shown in Figure 8. Air is fed through a FARR HP-2A class 2 type filter in the inlet section, into a centrifugal blower. The blower is powered by a Reliance 2.0 hp motor. A damper, made out of plexiglass, slides in an aluminum housing at the entrance to the inlet section. The damper restricts the amount of air ingested by the blower, thereby controlling the velocity of the flow. Once the air leaves the blower, it passes through a large settling chamber or plenum, with an interior volume of nearly one cubic meter. There is a baffle in the center of the plenum that directs the air to the sides of the chamber to help reduce any unsteadiness caused by the blower. The flow then passes through a shallow contraction and through the honeycomb and three screens. These are designed to reduce the freestream turbulence level and the mean swirl in the flow. A 2-D contraction with an area ratio of 4:1 transports the flow into the test section. There is a large roughness element at the entrance to the test section that produces a thick turbulent boundary layer far downstream (Saripalli and Simpson, 1980). The test section measures 194×23.5 cm. The height of the top wall varies along the length of the section to produce a zero pressure gradient flow.

At the end of the test section there is a plexiglass plate that extends the floor another 17.8 cm.

All of the flow measurements were taken above the plexiglass floor extension because there are no transparent portions of the test section floor. The maximum test section velocity attainable is approximately 24 m/s. The tunnel has a freestream turbulence intensity of 0.125%, measured 5.7 cm downstream of the roughness element (Smith, *et al.*, 1990).

2.2 Artificial Seeding

Flow seeding is very important for accurate and reliable velocity measurements. Seed particles, whether naturally occurring or artificially introduced, must act as infinitesimal fluid elements and follow the flow. The seeding material used in the current work was solid polystyrene latex spheres (manufactured at NASA Langley). The spheres are immersed in solution at a concentration of 1.26×10^{10} particles/ml (with 5 ppm Hexamine). The solution was diluted in ethyl alcohol (190 proof) at a ratio of about 50:1. The particles are 2.1 μm in diameter.

The design of the seeder that projects the particles into the flow is similar to a design by Chesnakas, *et al.* (1991). Figure 9 details the apparatus itself. It is made out of three tubes: one 1.27 cm diameter steel tube, and two 2.4 mm diameter brass tubes. The smaller diameter tubes are affixed onto the steel tube with a special high

strength epoxy that resists deterioration in alcohol (Dextor Hysol EA 934NA). Two plastic, flexible feeder tubes serve to carry the seeding mixture from a reservoir to the brass tubes. Compressed air is fed through a regulator into the large tube. Air is forced out through the hole in the steel tube which draws out the seeding liquid from the brass tubing. The air streaming out of the steel tube vaporizes the alcohol solution and the solid particles are expelled from the seeder. Although this seeder was originally designed for use in supersonic flows, it was found to work well enough in low speed flows for our purposes.

One other type of artificial seeding was tested with the prototype DAV: Di-octal phthalate (DOP). DOP is a popular seeding solution used with LDA. Once vaporized by compressed air it turns into an oily smoke that contains a large range of particle diameters. When using DOP for the flow seeding, the particle density in the measurement volume was too large for the prototype DAV (it saturated the detector). The smaller particle diameters also resulted in a poorer SNR.

2.3 Laser and Table

A 5 Watt Argon-ion laser (Spectra Physics model 164) was used as the non-intrusive probe. At a wavelength of 514.5 nm, its maximum output power is 2.2 W. It was assumed that the laser beam has a Gaussian intensity distribution. The laser rests on a stationary table made out of 1.27 cm thick aluminum supported by a frame

of aluminum C-channel. The table is mounted onto the traverse of a large milling machine. A photograph of this apparatus is shown in Figure 10. The milling machine provides a stable, vibration resistent base for the laser table. The traverse provides movement of the table in three mutually orthogonal directions. The milling machine rests on a wheeled cart which can be anchored into place.

2.4 Hot-Wire Equipment

Velocity profiles were measured at the test section exit using a TSI model 1210-71.5 single hot-wire probe. The hot-wire was connected to a Dantec constant temperature anemometer (model 56C01). The hot-wire's frequency response was flat out to about 7 kHz running at an overheat ratio of 1.7. Output from the anemometer went to a $\times 10$ zero-mean gain amplifier which was then read by an Epson AST computer using an Analogic 12 bit HSDAS A/D converter. The AST was operated using software written in house which enabled hot-wire calibrations and measurements to be made on line.

Flow temperature and pressure were recorded along with the velocity. A pitot-static tube in tandem with a Setra model 239 pressure transducer was used to sense the pressure, while an Omega digital thermometer (HH-25KF) was used for the temperature.

A computer controlled traverse that was originally designed and built for use

in the VPI & SU Stability Wind Tunnel was used to position the hot-wire. A long cylindrical probe stem attached to the traverse held the actual hot-wire device.

2.5 Health Precautions

Some safety precautions were taken to avoid inhalation of the seed material. Respirators with solid particle filters were worn, along with protective eye goggles that prevented accidental exposure to scattered laser light.

3.0 The Prototype DAV System

3.1 Description of the One-Component Prototype DAV

A schematic representation of the circuitry for the prototype is shown in Figure 11. A bi-cell silicon PIN photodiode with rectangular elements serves as the detector. Each photodiode has its own separate but identical analog circuit (henceforth referred to as channels). The photodiodes convert incident light energy into a current signal. This current signal is then converted to a proportional voltage and amplified. A voltage comparator amplifier produces a square pulse when it recognizes an analog voltage signal. The square pulses from each channel are input to the digital circuitry which measures the time that has elapsed between the pulses. The computer reads the elapsed time (along with other information) and waits for the next event (passage of a particle's image across the detector).

3.1.1 Sending/Receiving Optics

Figure 12 gives the co-ordinate system that is used for all direction references in this text. The positive X axis points downstream in line with the tunnel, the positive Y axis points vertically upwards, and the Z axis completes the right handed system. The optical setup for the prototype DAV is relatively simple because there is only

a single beam and a single detector. A schematic of the optical layout for the prototype is shown in Figure 13. The sending and receiving optics are completely contained within the YZ plane. The laser beam is directed by a beam steerer through a mask that blocks most of the stray light, across the measurement volume location above the plexiglass plate, and into a beam catcher.

The detector and the receiving optics are mounted to a framework that is rigidly attached to the laser table at an angle of about 45° with respect to the positive Z axis. A photograph of the setup is shown in Figure 14. The laser beam can be moved in any direction by using the milling machine's 3-D traverse. In this manner, the measurement volume and the receiving optics move together during a sequence of measurements.

The receiving lens for the prototype DAV is a Cosinon zoom macro mc camera lens with an aperture of 67 mm. The zoom capability of the lens can magnify images to more than twice their original size.

3.1.2 Detector and Amplification Circuitry

A bi-cell PIN photodiode from Silicon Detector Corporation (SD160-24-21-021) was chosen for the detector. As shown in Figure 15, it has two rectangular elements that make it suitable for 1-D time of flight measurements.

The measurement volume for the prototype DAV is defined by the optical setup and the dimensions of the detector array. For the work done in this study, the

measurement volume was 12.9 mm^3 large with a span-wise component length of nearly 8.5 mm.

The entire design for one channel of the amplification circuitry is shown in Figure 16. The primary stage amplifier is an inverting current-to-voltage converter, and the second stage is a voltage gain amplifier. The operational amplifier (op-amp) that is used for the primary stage is a Burr-Brown OPA627. The second stage amplifier is a Burr-Brown INA106 precision differential amplifier that provides a voltage gain of −10 (inverting). Power for this circuit, and all of the analog circuitry, is provided by a regulated differential 15 V supply.

Omitted from the diagram are the power supply connections to the amplifiers which are decoupled with 1 μF tantalum and 0.01 μF ceramic capacitors on the first stage op-amp. The second stage amplifier is decoupled with 1 μF tantalum capacitors.

To protect against radio-frequency and electrostatic interference, all of the analog circuitry was placed inside a shielded aluminum box. A small hole cut into the side of the box was fitted with a rubber grommet that houses the detector. All electrical signals are output from the box via four BNC cables (Belden RG 58A/U 8219).

3.1.3 Trigger Circuitry

The prototype DAV measures the time it takes for a particle's image to cross from one photodiode to the other. In order to do this, the signals produced by each half of the bi-cell must be digitally processed in some way. A 'trigger level' (constant

dc voltage level) is set manually prior to making a measurement. The analog voltage signals are compared to the trigger level with a comparator amplifier. The 'arrival' time of a signal is defined to be the moment that a signal crosses its trigger level. The output from the comparator amplifier is a square pulse which serves to mark a signal's arrival time. The time lapse between successive square pulses from each channel is the time of flight of a particle.

Comparator Amplifiers

A non-inverting Schmidt trigger circuit, made with a voltage comparator amplifier, is used to trigger on the amplified signals (Figure 17). The amplifier is a ¼LM339 quad comparator. The + input terminal receives the signal, and the - input terminal receives the trigger level. The comparator amplifiers are considered to be digital components and therefore share the digital electronics' power supply; two power supplies connected in parallel that produce +5 V and -1 V.

Signal Pre-Conditioning

The circuit that conditions the amplified signals and trigger level voltages for input to the Schmidt trigger is shown in Figure 18. The trigger level (V_{ref}) is created with a resistive voltage divider made of a 69.8 kΩ resistor and a 5 kΩ multi-turn potentiometer as shown. V_{ref} is variable between ground and -1 V. A Burr-Brown OPA2107 inverting, unity-gain, dual op-amp, creates a stable, relatively noise free (≈

2 mV_{p-p}) reference voltage out of V_{ref}. A Burr-Brown INA105 precision, unity-gain, differential op-amp is then used to subtract the reference voltage from the amplified signal. The trigger level for the analog signal is now its own ground line. The output from the INA105, along with its signal ground, are carried to the trigger circuit via a single co-axial BNC cable.

3.1.4 Digital Circuitry

Timing Circuit

The output from the trigger circuitry is a record of particle arrival times given by a train of square pulses. Looking at the diagram of the bi-cell photodiode (Figure 15), a logical order to the succession of the pulses can be determined. Assuming that there is only one particle in the measurement volume at any instant, then that particle's image will cross each of the photodiodes in turn. Obviously, 'valid' pulse trains arrive in pairs; one pulse from the leading diode's channel and one from the trailing diode's channel.

Measurement of the elapsed time between pulses is made with a free running 10 Mhz clock that drives four, cascaded, 4 bit binary counters. Prior to an event, the counters are set to zero. The first pulse in a valid pair of pulses starts the counters running, the second pulse stops the counters. The computer reads the 16 bit binary value that represents the time of flight of a particle, and resets the counters to zero in preparation for another event.

The timing circuit† shown in Figure 19 is designed to accept only valid pairs of pulses. For the purpose of explanation, let the first pulse in a pair of pulses come from the leading channel, and the second pulse come from the trailing channel. The first pulse sets the counters in motion and also closes the 'gate' that accepts signals from the leading channel. The second pulse stops the counters and shuts the 'gate' that accepts signals from the trailing channel. Once the computer has read the data from the counters, it rests them to zero and opens both of the 'gates' allowing for the next measurement.

All of the digital circuitry is made from low power TTL (transistor-transistor logic) parts.

Flow Direction Circuit

The order in which the two pulses enter the digital circuitry defines the sense of the calculated velocity. Output from the two halves of the timing circuit is directed to a 'set-reset' flip-flop made from two NOR gates. The flip-flop's output changes state when the order of the arriving pulses changes. This one bit of information is read by the computer along with the 16 bit counter value.

---

†Preceding the inputs to the AND gates (and following the outputs of the triggers) are two monostable multivibrators; one on each channel. They are not shown in the figure because they perform an obsolete function. All of the digital circuitry is positive edge triggered so there is no need to condition the output from the triggers.

3.1.5 Validation Circuit

The 'quality' of the analog voltage signals (their potential to provide a good velocity measurement) is judged by the validation circuit shown in Figure 20. The amplified signals from the two voltage gain stages are summed with an INA105 precision differential amplifier. The summed signal travels to two identical pre-conditioning circuits whose output goes to two separate trigger circuits (as described in section **3.1.3**) via BNC cables. One of the pre-conditioning circuits contains a preset upper dc voltage level for the validation process, and the other contains a preset lower dc voltage level. The remaining digital circuitry discriminates between the summed signals that have a peak magnitude between the two reference voltage levels, and those that don't. Only those signals whose combined magnitude falls between the two reference voltage levels are used for the velocity measurement. The output from the XOR gate is read by the computer along with the counter value and the velocity vector's sense.

3.1.6 Computer and Digital Interface

A Data Translation DT2817 digital interface board was used to transfer data from the prototype DAV's digital electronics to an IBM PC/XT compatible computer, and to transmit control commands from the computer back to the prototype DAV. The DT2817 has 32 I/O lines that are configured into four ports of 8 bits each. Each port can be separately programmed for input or output. This board is inexpensive and accordingly is rather slow. The DT2817 achieves a throughput of about 1 kHz

per port. A 50 pin ribbon cable transports the data from the DT2817 to the digital electronics. A compiled BASIC program controls the operation of the digital board.

3.1.7 Example of How the Prototype DAV Processes an Optical Signal

Figure 21 demonstrates the progressive steps by which the prototype DAV converts a particle image's incident light power into a form suitable for a time displacement measurement. Part (a) of the figure shows the signals as they pass through the analog and digital circuitry. Part (b) of the figure shows the signals as they pass through the validation circuitry. The vertical dotted lines represent exact correlations in time between specific points among the plots.

In Figure 21(a), one column shows the response of one channel of the prototype's circuitry, and the other column shows the response of the other channel's circuitry. The first plot is an example of the light intensity that is incident on the detector. The second plot shows the output current signals from the bi-cell as the image sweeps over the detector. The third plot is of the amplifier outputs. At this point, the signals from each channel are routed to the validation circuitry (Figure 21(b)). The fourth plot shows the voltage signals after their trigger levels have been subtracted out. The fifth plot is of the two trigger circuits' output. The comparators switch 'high' when a signal passes above its ground, and then switch 'low' when the signal falls below ground. The last plot shows the monostable multivibrator outputs that are used to make the time of flight measurement. The time of flight of the particle is $t_2 - t_1$.

In Figure 21(b), the two separate trigger circuits of the validation circuitry are shown in a single column. The first plot is the sum of the two amplified voltage signals. The second plot shows the low validation trigger's output, and the third plot shows the high validation trigger's output. The last plot is the XOR gate's output which is read by the computer to determine the quality of the signal pair.

3.2 Measurements Made With the Prototype DAV

Rotating Disk Measurements

To facilitate a velocity measurement under controlled conditions, the prototype DAV measured the speed of a very thin wire attached to a rotating plexiglass disk as it passed through the laser beam. The circular disk was attached to a shaft powered by a small motor mounted over the measurement volume. A 0.13 mm diameter wire taped to the edge of the disk simulated a seed particle in the flow. The disk's speed of rotation was controlled by a variable autotransformer that supplied ac voltage to the motor driving the disk. The disk had a maximum rotation rate of about 28 Hz.

A semi-independent measure of the wire's speed was made with a frequency counter. The amplified voltage signals from the analog circuitry were routed to a $\times 10$ 'buck and gain' amplifier and then to a function generator with a 'phase lock' capability (Tektronix FG501). The FG501 produced a square pulse that triggered on the rising edge of the input analog signal. The square pulse was then input into a Data Precision

frequency counter (model 5740) that measured the frequency of rotation of the disk with an accuracy of ±0.05 Hz. The wire's velocity was calculated from the disk's angular velocity and the distance between the wire and its center of rotation.

Flow Measurements

The prototype DAV also made velocity measurements in a seeded flow with a freestream velocity of 10 m/s. The location for the measurement profile was 11.7 cm downstream of the test section exit above the plexiglass floor extension in the spanwise center of the flow.

3.3 Design Considerations

This section presents a more detailed and in depth look at all of the aspects concerning the design of the prototype DAV. The optical components are discussed first, followed by a discussion of the electronic circuitry. The individual circuits themselves were designed to adequately perform specific tasks. In general, no attempt was made to bring the designs to an 'optimal' state.

3.3.1 Scattered Light Power

The position of the detector relative to the flow direction is given by the two angles ϕ and ψ. Referring to Figure 13, the elevation angle (ϕ) is measured as a positive

rotation about the Z axis with $\phi = 0^{\circ}$ pointing in the negative X direction (out of the plane of the paper). The orientation angle (ψ) is measured as a positive rotation about the X axis with $\psi = 0^{\circ}$ pointing in the positive Z direction (as shown in the figure).

The magnitude of the scattered light power received varies drastically with the orientation angle chosen. The variation in scattered light power (P_s) with respect to the orientation angle (for three different receiving lens' diameters) was calculated using a computer program called STREU (Naqwi and Durst, 1989). The program estimates the P_s with a given set of initial conditions for various laser velocimetry applications. The program can use either Mie theory or a geometrical theory to compute the properties of reflected and refracted monochromatic light. For the results presented here, Mie theory was used.

The input parameters were chosen to approximate the actual conditions of a flow velocity measurement made with the prototype DAV. Laser power was set at 1.5 W with a beam diameter of 2 mm and a wavelength of 514.5 nm. Scattering particles were spherical with a diameter of 2.1 μm. The receiving optics were circular: diameters of 2.54 cm, 5.08 cm, and 7.62 cm were input to the program. The distance between the plane of the receiving optics and the measurement volume was 15.24 cm.

Figure 22 shows the results from STREU. Scattered light power decreases as the orientation angle increases until $\psi \approx 110^{\circ}$. As ψ increases further, the scattered light power rises. To collect the most light, the receiving optics should be in the forward scatter mode (preferably with $\psi < 45^{\circ}$). Flow velocity measurements in this study were

taken with an elevation angle of 90°, and an orientation angle of about 45°.

The actual light power received by the prototype DAV (judged by the analog signal levels being triggered on) was between 1.25×10^{-8} W and 1.75×10^{-8} W. According to the calculation by the program STREU, the received scattered light power should be about 1.5×10^{-8} W (for an aperture of 67 mm). These values compare very favorably and therefore seem to validate the results presented in Figure 22.

3.3.2 Sending/Receiving Optics

Size and Shape of the Measurement Volume

All of the measurements made with the prototype DAV in this study were done so with the plane of the detector parallel to the plane of the receiving lens. Figure 23 shows the shape of the measurement volume when the receiving lens is at a distance of one focal length from the laser beam. The measurement volume is a slice from the center of a circular cylinder in the shape of a parallelogram. The base of the volume has a length of $l_d/\sin\psi$ where l_d is the length of the bi-cell. The height of the volume is the diameter of the laser beam, and the width is necessarily the width of the bi-cell. As the orientation angle decreases (amount of forward scatter increases) the overall length of the measurement volume increases, but its volume does not change; that is fixed by the size of the detector array and the diameter of the laser beam.

Receiving Lens Magnification

The amount of magnification used in the receiving optics can greatly affect the way the prototype DAV operates. The main parameters that can be altered are the size and shape of the measurement volume, and the resolution of the prototype.

Increasing the magnification in the receiving optics has the effect of reducing the measurement volume size. Magnifying the image 2 times will decrease the dimensions of the measurement volume by $1/2$, and decrease its volume by $1/2^3$.

A drawback to incorporating magnification into the receiving optics is that it reduces the maximum measurable velocity of the instrument. A particle passing through the measurement volume at a velocity of u m/s that has been magnified M times, moves at a speed of $u \times M$ m/s relative to the detector. Therefore, the maximum velocity that the prototype DAV can accurately measure is reduced by a factor of M.

The prototype's velocity resolution also suffers with increased magnification. If the effective particle velocities (relative to the detector) are higher, then the measured time of flight will be shorter. Because of the finite clock speed that drives the counters, shorter time of flight measurements are made with less accuracy. For example, a particle travelling with a true component velocity of 10 m/s measured with $M=1$, has a resolved accuracy of ± 0.02 m/s. That same particle measured with $M=2$ has a resolved accuracy of only ± 0.04 m/s. Thus, the prototype DAV's velocity resolution at a given flow speed is decreased by a factor of M.

Sending Optics

Inserting a converging lens in the path of the sending beam can reduce the size of the measurement volume and increase the prototype's SNR. The light power contained within the measurement volume increases in proportion to the square of the reduction in beam radius. Thus, the SNR increases by the same amount. This could be important in a system that uses a less powerful laser than the one that was used here. Focusing the laser beam will also decrease the size of the measurement volume in direct proportion. The beam diameter may be reduced as much as desired so long that the beam's image completely covers the photodiodes.

A double-convex lens with a focal length of 400 mm was tested as a focusing lens for the prototype DAV. It was discarded after the realization that the increase in light power was unnecessary.

3.3.2.1 Alternative Receiving Lenses

Before the camera lens was adopted for the receiving lens, two other types of lenses were tried: a double-convex glass lens and a fresnel lens. They are worth discussing here because they unequivocally show the need for high quality optical components. For the purposes of comparing the different lenses, it is prudent to discuss the camera lens first.

Camera Lens

Plots of analog signals produced by the prototype DAV when measuring the speed of the wire on the rotating disk using the camera lens as the receiving lens are shown in Figure 24. The figure details a pair of signals produced by a single pass of the wire through the measurement volume. Each horizontal division on the graph represents a 50 mV difference, and each vertical division represents a time displacement of 20 μs. These signals were captured with a digital oscilloscope (Tektronix model 2211). The binary data was then transferred to the computer via software provided by Tektronix.

An 'idealized' pair of analog signals might look like those shown in Figure 21. The two signals of Figure 24 approximate square pulses to some extent, with fairly steep leading and trailing edges, but their peaks are sharply pointed. The reason for this could be the changing light intensity distribution of the image. Also, the shape of the wire's image changes as it passes over the photodiodes because the wire rotates with respect to the detector as it moves across the measurement volume. The peaks in the signals of Figure 24 may also be affected by the intensity distribution of the laser beam.

Compound Lens

The first of the alternative lenses tried was a compound double-convex lens composed of two plano-convex glass lenses placed back-to-back. Each single lens had

a focal length of 25.4 cm and a diameter of 15.24 cm. The effective focal length of the compound lens was 12.7 cm. The attractive feature of the compound lens was its large diameter that gives it the ability to collect a large amount of scattered light.

Analog signals produced by the prototype DAV when measuring the speed of the wire on the rotating disk using the compound lens as the receiving lens are shown in Figure 25. Horizontal divisions on this graph are in increments of 0.2 V, and the vertical divisions are 20 μs apart.

The most obvious differences between this graph and that of Figure 24, are the smoothness of these signals, their rounded peaks, and the apparent electrical or optical interference present on the leading edge of the second signal and the trailing edge of the first signal. The difference in the time delay between the two signals of Figure 25 and those of Figure 24 is due to a difference in receiving lens magnification.

The reason that the signals in Figure 25 appear so 'smooth' is the diffuse image cast by the compound lens. When the image of the wire produced by this lens was viewed on a white piece of paper placed at its focal point, a large halo of scattered light was seen surrounding and almost swamping the image.

The 'interference' seen in the signals could be electrical pick-up or cross talk between the two amplifier channels, or it might be an optical phenomena caused by the receiving lens. The fact that this interference does not appear in the signals of Figure 24 suggests that the problem is an optical one. In an effort to determine the cause of the interference, a mask was placed over the outer edges of the compound

lens. It was discovered that only the central portion of the lens was contributing to the formation of the image. A mask with a hole 3.8 cm in diameter, properly positioned over the lens, could remove most of the interference from the leading edges of the signals. Analog signals produced with a mask over the compound lens are shown in Figure 26. The fact that this interference can be removed by masking parts of the receiving lens strongly suggests that it was an optical phenomenon, and not an electrical one.

Fresnel Lens

A high quality Oriel fresnel lens with an active diameter of 10.16 cm and a focal length of 12.7 cm was also tested as a receiving lens. Fresnel lenses are inexpensive and fairly rugged when compared to other quality lenses. However, they are not used in applications where coherence is important (such as LDA). A fresnel lens does not preserve the time dependent nature of the light wave because it does not produce equal ray path lengths between the object and the image. For the DAV, a coherent image is not necessary, but a sharply focused one is. The image produced by the fresnel lens was no better than that of the compound lens. It was blurred and surrounded by reflections from the grooves in the lens.

3.3.3 The Detector and the Current-to-Voltage Converter

A photodetector is a device that is designed to convert optical energy to electrical

energy. The silicon PIN photodiode does this with a higher quantum efficiency than is possible with an avalanche photodiode (Durst, *et al.*, 1976). The PIN photodiode, however, has no internal amplification so amplifier(s) must be added externally. The decision to use PIN photodiodes for the detector was governed mainly by the ease in which they can be segmented into a small array.

For the prototype DAV, the capability to measure one component of velocity was desired. A minimum of two photodiode elements are needed to make a one component measurement. A rectangular array of two photodiodes (a bi-cell) was chosen for the detector because of its low cost.

A PIN photodiode converts light power to a proportional current. The output signal current has a linear relationship to the incident light power. To maintain this linear relationship the voltage across the diode must remain constant. Constant voltage is most easily achieved by attaching the cathode of the photodiode to a signal ground, and connecting the anode to the virtual ground of an op-amp (see Figure 16). Monitoring the diode in this manner, the amplifier is said to be a current-to-voltage converter.

The incident light energy on the detector is of the order of magnitude of 10^{-8} W (see section **3.3.1**). The photodiodes will convert about one fifth of this energy into a current (the radiant sensitivity of the photodiodes at 514.5 nm is about 0.2 (Silicon Detector Corp., 1984)). A signal gain of 100 million is needed to boost this current to a useable voltage level. Using a single feedback resistor to achieve the entire gain could cause difficulties in obtaining the desired amplifier response characteristics.

The first thing that was done was to spread the total signal gain over two stages. The feedback resistor for the primary stage was chosen to be as large as possible, providing the most current-to-voltage gain, while still allowing ample signal bandwidth. The second stage amplification circuitry is discussed in section **3.3.4.**

The main difficulty encountered with high valued feedback resistances is achieving a balance between the desired current-to-voltage gain, and the desired signal bandwidth. Increasing the size of the feedback resistor reduces the signal bandwidth by an inverse relationship: $\Delta f \propto 1/R_f$. Parasitic capacitances are also common around large feedback resistances and can severely reduce the available signal bandwidth. To protect the circuit from external noise sources, the amplification circuitry was enclosed in a shielded metal box. A frequency response of 100 khz was sought, and a value of 10 MΩ was chosen for the feedback resistor.

3.3.3.1 The Prototype DAV's Dynamic Response Characteristics

The dynamic response characteristics of the prototype were determined by simultaneously exciting both photodiodes with a green light emitting diode (LED). A sinusoidally varying voltage plus a dc offset voltage were used to drive the LED (Hewlett Packard HPMP-3507) as it was swept over the frequency range of 100 Hz to 10^5 Hz (which is well within the frequency response of the LED). A Tektronix FG501 function generator provided the variable voltage.

The dynamic response of the prototype DAV is governed by the first stage

amplifier. Figure 27 is a plot of the circuit's normalized frequency response (in decibels) between 100 Hz and 10^5 Hz. The cutoff frequency of channel 1 (defined as the frequency at which the normalized response is equal to -3 dB) is ≈ 78 kHz. Channel 2's cutoff frequency is ≈ 88 kHz. The response of both channels is equivalent up to frequencies of 10 kHz. At frequencies greater than 10 kHz, channel 1 experiences signal gain peaking that reaches a maximum of about 25% at 50 kHz. The response of channel 2 is flat (± 0.5 dB) out to 60 kHz where it starts to roll off. Signal gain peaking of high feedback resistance current-to-voltage converter circuits is discussed in Burr-Brown, 1987.

The circuit's phase characteristics are shown in Figure 28. The plot is of lagging phase (in degrees) vs. frequency for each channel. The two curves are very similar, with a response at -90° of 53 kHz for channel 1, and 62 kHz for channel 2.

3.3.3.2 Interfering Effects

Signal Noise

Nothing had a more dramatic effect on the circuit's output noise (e_n) than the choice of the power supply. Four different power supplies were tested in conjunction with the prototype DAV. Each supply had a similar ac noise level when operated with no load. However, the prototype's output signal noise varied greatly among the different supplies. Figure 29 shows the ac-coupled noise riding on the positive dc voltage line of each power supply. Figure 30 shows the circuit output noise for each power supply. The power supply used with the analog circuitry of the prototype DAV is power

supply "C".

The output circuit noise was measured by taking four 4000 byte samples with the digital oscilloscope and averaging them. The rms noise level of channel 1 at the output of the second stage amplifier is 8.9 mV, and the rms noise level of channel 2 is 9.2 mV.

Non-Identical Circuit Channels

The differences in the dynamic response between the two amplifier channels result from unmatched gains, unsymmetrical component layout geometry, and unequal amounts of stray capacitance in the feedback network of the primary stage. The feedback resistors in each channel are not precision resistors and may differ by as much as 4%. The physical positioning of the components on the printed circuit (PC) board affected the circuit's dynamic response. The architecture of the two channels was kept as symmetrical as possible because of this. Physical symmetry between the two circuits is most important in the primary stage. The relative positions of the feedback resistor and the power supply decoupling capacitors could change the frequency response of a circuit channel by as much as 50%, and the amount of gain peaking by 300%.

The effect that component positioning has on the gain peaking of the circuit is emphasized in Figures 31 and 32. Here, the feedback resistors of the first stage amplifiers were placed flush against the PC board. Figure 31 is a plot of normalized response vs. frequency, and Figure 32 is a plot of phase lag vs. frequency. The capacitive

coupling between the resistors and the current-to-voltage amplifiers is much greater and results in a 75% peak magnitude response in the signals at a frequency of about 60 kHz. The characteristics of the two channels of Figures 31 and 32 are much better matched than those of Figures 27 and 28. This shows that by increasing the physical similarity between the two amplifier channels, their dynamic responses become more alike.

After the circuitry for the prototype DAV had been built, it was discovered that the differences in dynamic response between the two channels did not affect the prototype's accuracy in measuring velocity. For this reason, no attempts to equalize the response between the two channels were made.

3.3.3.3 Theoretical Noise Calculations

An attempt was made to find the theoretical noise limit for the first stage of the amplification circuitry. This noise level is also approximately the limit posed for the entire analog circuit because almost all of the signal noise is generated in the current-to-voltage amplification stage.

To study the noise output from an amplifier circuit, it is useful to model actual op-amp behavior with a perfect 'noiseless' amplifier plus its modifying inputs. Figure 33 is an equivalent noise circuit for the first stage. e_n represents the ac output voltage noise, calculated from the formula (Durst, *et al.*, 1976; Dowling, *et al.*, 1989; Wong, 1976)

$$e_n = \left(\sqrt{\overline{i_d^2}} + \sqrt{\overline{i_a^2}}\right) R_f$$

where,

$$\overline{i_d^2} = 2q(I_o + I_p)\Delta f + \frac{4kT\Delta f}{R_d}, \quad \overline{i_a^2} = 2q i_b \Delta f + \frac{4kT\Delta f}{R_f}.$$

In this equation, I_o is the photodiode dark current [A], I_p is the mean photon current [A], Δf is the signal bandwidth [Hz], i_b is the amplifier input bias current [A], T is the temperature [°K], R_d is the photodiode resistance [Ω], R_f is the feedback resistance [Ω], q is the elementary charge of an electron (1.6×10^{-19} Coulombs), and k is the Boltzman constant (1.38×10^{-23} J/°K).

For input values of $I_p = 3$ nA, $I_o = 1.5$ nA, $i_b = 10$ pA, $R_d = 500$ MΩ, $R_f = 10$ MΩ, $\Delta f = 85$ kHz, and $T = 300$ °K (Burr-Brown, 1989; Silicon Detector Corp., 1984); e_n is equal to 0.23 mV_{rms}. The mean photon current was calculated using the formula $I_p = P_s \times k_r$, where P_s is the scattered light power incident on the detector (from Figure 22), and k_r is the radiant sensitivity of the diodes. The value of k_r is an extrapolation from the data provided in the reference source of Silicon Detector Corp., 1984. Notably, the error bands on I_p are wide (± 15%).

The greatest contributors to the signal noise are the photodiode shot noise $2q(I_o + I_p)\Delta f$, and the thermal (Johnson) noise of the feedback resistor $(4kT\Delta f)/R_f$. Thermal noise from the photodiode resistance is negligible, as is the amplifier shot

noise. The mean photon current (I_p) is the dominant factor in the diode shot noise. The dark current (I_o) is given by the manufacturer, but it increases with the age of the photodiode and could be as great as two or three times that of the quoted value.

The measured value of e_n was $\approx 0.9\ mV_{rms}$ (for the first stage amplifier), which is four times larger than the estimated theoretical value. Probably the main reason for the discrepancy is the uncertainty in I_o and I_p. Also contributing to the larger noise value are unwanted coupled noise currents that arise from the imprecise construction of the circuit.

3.3.3.4 Other Primary Stage Amplifier Circuits Tested

Some other circuits that use a current-to-voltage converter to monitor the photodiodes were tested before the present design was adopted. A few of the ideas that were pursued are presented here.

Originally, a Burr-Brown OPA637 amplifier was used for the current-to-voltage converter because it has a larger open-loop bandwidth than that of the OPA627. Many different values for R_f were tried in the feedback network in an effort to maximize the gain without losing all of the frequency response. With a feedback resistance of 2 MΩ, a signal bandwidth of 400 kHz was achieved with an output noise of 10 $mV_{p\text{-}p}$. This would be equivalent to 50 $mV_{p\text{-}p}$ noise at a current-to-voltage gain of 10^7 (which is almost ten times the amount of noise in the present circuit). To reduce the noise, a variety of high and low-pass (passive and active) filters were added to the amplification

circuitry to decrease the signal bandwidth; none of which successfully reduced the noise without practically eliminating the frequency response. Another way of reducing the noise is to add capacitance in parallel with R_f. A tunable sub-picofarad capacitor 'tee' was placed around the feedback resistor. It was found that reducing the noise in this manner choked off the frequency response of the circuit faster than did adding filters to the op-amp's output.

The OPA637 often became unstable when powering up, swinging rail-to-rail at its output. The OPA637 is designed to be stable in gains ≥5 (Burr-Brown, 1989), where the OPA627 is unity-gain stable. The current-to-voltage converter circuit has a voltage gain of $-Z_f/Z_d$ which is less than or equal to unity at the frequencies of interest. For this reason the OPA627 was chosen in place of the OPA637.

Modifications to the basic circuit design of Figure 16 were tried to improve its characteristics. Reverse biasing the bi-cell photodiode only increased the output noise without showing any significant improvements to other characteristics (e.g., frequency response, phase response, etc.). A resistor was placed between the + input terminal and ground to try to match the error voltages at the amplifier inputs due to the amplifier bias currents. This caused the amplifier to go unstable.

3.3.4 Second Stage Amplifier

A net transimpedance of 100 MΩ was desired for the amplification circuitry. The total gain was spread over two stages: the first is a current-to-voltage gain of

10^7, and the second is a voltage gain of 10. The addition of a small voltage gain after a large current-to-voltage gain boosts the output signal strength without decreasing the SNR. This is possible because the signal acquires most of its noise from the primary stage. The net transimpedance of the entire circuit is now defined as the product of the current-to-voltage gain from the primary stage, and the voltage gain from the second stage.

Some different op-amps were tested for the second stage. It was found that so long as the amplifier had sufficient bandwidth, the output noise of the circuit was the same no matter what amplifier was used. An LM318 op-amp and an OPA627/637 op-amp had the same effect on the output noise of the circuit.

One disadvantage to using the LM318 amplifier was the large relative voltage offset that occurred between the two channels. A compensating potentiometer was needed to zero out the difference in dc voltage.

The INA106 was finally chosen for the voltage gain stage because of its compactness and its precision fixed gain. Using INA106s also eliminated the offset voltage problem.

3.3.5 Example Analog Signals

Pairs of analog signals produced by the prototype DAV from measurements made in the freestream of a seeded flow are shown in Figure 34(a-d). The signal traces shown in Figure 34(a) were taken with a very low seeding concentration so that the

signals would stand out against the background noise. Both signals rise very quickly as the particle's image first crosses onto each diode, they peak at a roughly constant level while the image is crossing over the diodes, and then fall when the image leaves the diodes. Notice the small 'spike' on each of the signals, one preceding the leading edge of the first signal, and one after the trailing edge of the second signal.

Figure 34(b) is more representative of a 'good' pair of signals. This figure shows the level of background noise that accompanies the signals during a measurement. Also in this figure is the detection of a particle that crossed through the outer edges of the measurement volume. Figure 34(c) is a pair of signals that would be considered 'poor' in quality. These signals do not have parallel leading edges with steep slopes and therefore would cause an error in the time of flight measurement. The accuracy to which the prototype can measure the velocity depends heavily on the quality of the signals it produces. Signals like those in Figure 34(c) are the largest cause of error in the time of flight measurement. The distribution of 'good' and 'poor' quality signals is about half and half.

Figure 34(d) is a plot of a pair of signals that have overwhelmingly large spikes riding on them. Signal spikes like these occur on about a third of all the 'good' signals that the prototype DAV produces. The cause of these spikes is unknown. The spike on the leading edge of the first signal is often large enough to pass through the trigger voltage level for that channel. When this occurs, that velocity measurement is biased low. This can introduce a significant error into the measurement of mean velocity.

What is known about this phenomena is the following: 1) when the spikes do appear on the analog signals they always occur in the same pattern — one large spike on the leading edge of the first signal and one smaller spike on the trailing edge of the second signal, 2) the spikes are only noticeable when the camera lens is used for the receiving lens. These facts lead to certain conclusions about the problem. The spikes can not be a part of the seed particles' true image because if they were, then the spikes would appear symmetrically about the signals and not asymmetrically. For the same reason, the spikes could not be part of the laser beam's intensity distribution. They are not caused by an oscillation or any other peculiarity from the amplification circuitry because the first spike appears before an event takes place. Since they only appear when the camera lens is used, they are only visible when the particles' images are sharply in focus with the detector array.

3.3.6 The Analog to Digital Interface

The reason for the seemingly elaborate scheme (section **3.1.3**) of preparing the amplified signals for triggering is simple. Impedance matching is very important throughout the analog circuitry, especially at the interface between the analog and digital circuitry. The comparator amplifier has a relatively low input impedance. Therefore, the impedance presented to the comparator amplifier inputs by the signals must be extremely low. An output impedance of 0.01 Ω is provided by the INA105 difference amplifier. The INA105's common mode rejection ratio is 90 dB. Thus,

by subtracting the trigger level voltages from the amplified signals, any coherent noise between the two is also subtracted out.

The analog circuitry had to be kept completely separate from the digital circuitry, both electrically and physically. Any signal transfer between the two occurred in an 'isolated' manner. There are no single ended inputs and no signal ground or power connections between the two circuits. The INA105 amplifier makes this possible by creating a voltage signal that uses its own ground for its trigger level, providing a differential input for the Schmidt trigger.

3.3.7 The Validation Scheme

The triggering scheme for the prototype DAV (section **3.1.3**) was chosen because it was the simplest design possible for measuring the time of flight. However, with only a single point on each analog signal to establish arrival time, many errors are introduced because of 'poor' quality signals. It is also important to ensure that the comparator amplifiers trigger on the steepest part of the signals. This is necessary for the prototype DAV to make accurate time of flight measurements. For the single trigger point scheme to be effective, a method for determining signal quality must be devised. The validation circuitry of section **3.1.5** is such a method.

The combined magnitude of the signal pair is compared to the predetermined validation reference voltage range. If it falls between the two set levels then that signal pair is considered to be 'good'. The sum of the signals from the two channels is used

because it cuts down on the amount of circuit components needed. It would be better to sample and compare each of the signals in the pair but that would take twice as much circuitry. Using the summed signal for the validation process is a compromise between efficiency and effectiveness.

Setting the validation voltage levels defines the 'good' range for the analog signals' strength. Seed particles that pass through different parts of the laser beam will produce signals of different sizes due to the intensity distribution of the beam. Placing the validation levels correctly can ensure that the validated signal pairs correspond to particles that passed through the center of the laser beam. In fact, if the intensity distribution of the laser beam is known, the validation voltage levels can be used to reduce the effective beam diameter thereby reducing the size of the measurement volume. Also, if the trigger voltage levels are set below the validation reference levels, then necessarily the triggers will trigger on the rising edges of the signals and not the 'flat' peak of the signals.

Choosing signals for more accurate velocity measurements should involve measuring the rise time of the leading edge of each signal, and the degree of parallelness between the two leading edges. One way to do this would be to use a number of different trigger levels (three or more). Then the slope of the rising edge of each signal could be compared to a preset value to determine whether or not that signal should be validated. A more efficient way of accomplishing the same thing would be to digitize the prototype DAV's signals with a high speed A/D converter. Then any number of

different triggering schemes might be employed by a computer program.

3.3.8 The Digital Interface Board

All the lines emanating from the digital board have a small dc voltage impressed upon them by the computer that disrupted the counters' ability to change output states properly. TTL hex Schmidt triggers were placed between the counter output lines and the digital board. The hex Schmidt triggers effectively eliminated errant switching in the counters.

4.0 Velocity Measurements & Discussion

4.1 Sources of Bias Error in Measurements Made with the DAV

The following is a discussion of errors that affect the DAV concept as well as the prototype. However, many sources of error are only relevant to the prototype DAV. These are discussed in section **4.1.3**.

4.1.1 Rise Time and Noise

The electrical noise riding on the amplified signals produces an error in the DAV's calculation of velocity. The peak-to-peak magnitude of the noise coupled with the slope of the leading edge of a signal defines the error due to signal rise time and noise. The peak-to-peak noise level, $e_{n(p\text{-}p)}$, is defined as the ac voltage that bounds 99.7% of all possible voltage noise values (for a Gaussian noise distribution). $e_{n(p\text{-}p)}$ is therefore equal to $\pm 3\sigma$, where σ is the standard deviation (in volts) of a probability density distribution of the noise.

An idealized voltage signal with a noise level of $e_{n(p\text{-}p)}$ is shown in Figure 35. The slope of the leading edge of the signal at the trigger point is given by $m = V_t/\tau_r$, where V_t is the 'rise' of the signal in Volts, and τ_r is the 'rise' time. The error resulting from measuring the time of flight between two identical signals is $\delta t = e_{n(p\text{-}p)}/m$. Values

for σ were calculated as 8.9 mV for the first channel and 9.2 mV for the second channel. For a typical 'good' pair of signals, V_t is about 150 mV and τ_r is 5 μs. After averaging the two values for σ together, δt is equal to ± 0.9 μs.

4.1.2 Geometry of the Detector Array

Some of the error in the calculation of velocity will result from the shape of the photodetector array. To make accurate measurements with the prototype DAV, it is essential for the particle's image to cross the leading edge of both diodes. By looking at Figure 15, it is obvious that there are two possible image paths across the detector that will produce erroneous velocity measurements: (1) a particle image that clips the edge of one diode and then crosses the leading edge of the other diode, (2) a particle image that crosses one diode but not the other. In a highly turbulent flow, much of the error would also be the result of particles traveling toward and away from the detector.

Assuming there is only one particle image passing over the detector at any instant (which is a necessary condition for the prototype DAV's operation anyway), then the time between events will be large compared to the time of flight of a particle. Therefore, errors due to (2) will produce velocities very near to zero. This may only be a problem if the mean velocity itself is near zero. Errors due to (1) may bias the mean velocity high because of the shorter distance the image travels across the array.

In actuality, the effects of the bias error due to array geometry are negligible

in the present study. For the turbulent boundary layer generated at the exit of the small wind tunnel, there is little span-wise flow. If it is assumed that 99% of the fluid particles travelling through the measurement volume have a flow angle relative to the positive X axis of less than 15° (in a horizontal plane), then approximately 3% of the sample particle velocities will have a bias due to error source (1). If the particle images in this small percentage cross over the edge of the bi-cell in an equal dispersement of initial contact positions so that each particle image travels a different distance, then only one fifth of those particle velocities will add into the calculation of the mean velocity. Any image that travels a distance of less than 0.4 mm from diode to diode will produce a velocity large enough so that it falls out of the $\pm 3\sigma$ range for all of the velocity samples. Therefore, for a particle-averaged mean velocity calculated from 1000 samples, only 6 of those samples would be biased high.

4.1.3 Sources of Bias Error Inherent to the Prototype DAV Only

Velocity Gradient

There is a small bias error incorporated into the prototype's velocity calculations because of the limited positional accuracy of the prototype DAV and the velocity gradient in the boundary layer close to the wall. This type of error is common to many velocimeters. For the mean velocity measurements made with the prototype DAV in this study, the bias error due to velocity gradient has a maximum nearest the wall of $\pm 0.5\%$ (relative to the freestream velocity).

Velocity Resolution

There is a limit on the accuracy of the prototype DAV imposed by the timing scheme used for measuring the time of flight. The speed of the free running clock within the digital circuitry defines the upper limit on the accuracy of the velocity measurements. This limit is exactly the velocity resolution (which varies with the value of the measured velocity). For the mean velocity measurements done in this study, the maximum error due to resolution is ± 0.02 m/s.

Signal Spiking

An unknown phenomena causes spikes to appear on the amplified signals when the images are sharply focused onto the detector. The signals shown in Figure 34(d) are a good example of this. If the channel triggers on the spike and not the true signal, the prototype's mean velocity calculation could be biased low. Also, this would increase the measured turbulence intensity. The velocity probability density distributions for the profile measurements done in this study (Figure 40) do not have a noticeable velocity bias in them. For this reason, it is believed that the signal spiking does not result in any significant contribution to the error in measuring the mean velocity or the turbulence intensity.

Before the measurements in the boundary layer were taken, the trigger level voltages were set through a trial and error process to assure that the comparator amplifiers would not trigger on the signal spike too often. Towards future work, it

is of primary importance to find the cause of these spikes and eliminate them.

Trigger Misfires

The noise that accompanies the amplified voltage signals causes the Schmidt triggers to 'fire' many times on the same signal. This phenomena is detailed in Figure 36. As the signal crosses back and forth over the reference voltage level, the trigger outputs a series of square pulses. The digital electronics is designed to compensate for this, to a small degree, by shutting off the input gates to the timing circuitry after the first pulse is encountered. The turn around time for this operation is about 100 ns which is not quite fast enough to stop the multiple pulses from interfering with the timing circuitry. The result of the multiple triggering can be seen in the velocity histogram of Figure 37. The small bump in the right half of the figure is the correctly measured velocity, and the enormous spike at the 0 m/s location is erroneous velocity data caused by the multiple trigger pulses.

This source of error could be reduced by allowing the Schmidt triggers to trigger over a zone of 50 mV or so with the proper amount of positive feedback. One way to eliminate this problem would be to digitize the amplified signals with a fast A/D converter. This would allow the time of flight measurement to be taken by any number of computer software related means eradicating the need for electronic triggers.

Spatial Averaging

The prototype DAV, in concept, is a point velocity measurement device. The prototype's measurement volume comprises 12.9 mm^3 of space, with a span-wise component length of nearly 8.5 mm. The velocity measured with the prototype DAV is a particle-averaged quantity (opposed to a true time-averaged quantity) that is also spatially averaged over the entire width of the measurement volume.

In principle, the prototype DAV's spatial resolution could be substantially improved by reducing the size of the photodetector array. The bi-cell photodiode that is used with the prototype was chosen because of its availability and its low cost, not its geometrical characteristics. Increasing the receiving lens magnification and reducing the laser beam diameter would also decrease the size of the measurement volume thereby increasing the spatial resolution.

4.2 Sources of Uncertainty in the Present Velocity Measurements

4.2.1 Prototype DAV

The major sources of uncertainty in the prototype measurements are the magnification factor for the receiving optics, the unsteadiness in the freestream velocity, and possible non-parallel leading edges of the amplified signals. The magnification factor was determined after the profile measurements were taken by comparing the freestream velocity measured by the prototype DAV to the freestream velocity measured

by the pitot-static tube. The magnification factor was 1.069 ±0.01. The small change in the dynamic pressure of the flow caused a variation in the freestream velocity of ±0.06 m/s. Signal pairs with non-parallel leading edges would cause an error due to the placement of the trigger level voltages. Most of the pairs that qualify as 'good' have a high degree of parallelness between the signals. Uncertainty due to leading edge non-parallelness is certainly small and is not considered in the uncertainty analysis.

An uncertainty analysis was performed on the prototype DAV's velocity measurements (presented in section **4.5**) using the method described by Kline and McClintock (1953). The parameters discussed in this section as well as those of section **4.1** were taken into consideration. The uncertainty in u/u_{ref} is ±4.6% at the first point in the profile and ±2.8% at the last point in the profile. The uncertainty in $\sqrt{\overline{u'^2}}/u_{ref}$ is ±1.6% at the first point in the profile and ±3.7% at the last point in the profile. The effects of particle-averaging on the velocity were not considered.

4.2.2 Hot-Wire Anemometer

The main parameters that effected the accuracy of the hot-wire measurements were the calibration constants in the King's law equation (Blackwelder, 1981), the unsteadiness in the freestream velocity, and the velocity gradient in the boundary layer. Uncertainty in the freestream velocity for the hot-wire measurements was estimated to be ±0.03 m/s.

Again, the method of Kline and McClintock (1953) was used to estimate the accuracy of the hot-wire's measurements. The uncertainty in u/u_{ref} is $\pm 1.3\%$ at the first point in the profile and $\pm 1.2\%$ at the last point in the profile. The uncertainty in $\sqrt{\overline{u'^2}}/u_{ref}$ is $\pm 0.6\%$ at the first point and $\pm 1.6\%$ at the last point.

4.3 Operation of the Prototype DAV

The prototype DAV does not need to be calibrated in the strictest sense of the word, but the detector does need to be properly aligned with the image of the measurement volume. The image plane must be well focused onto the detector for the velocity measurements to be as accurate as possible.

The trigger and validation reference voltage levels must be set manually. Determining the correct values for these levels involves taking velocity measurements in a known flow condition, and optimizing the levels through a trial and error process. This could be considered a 'calibration' of the prototype since it must be done within a known or predetermined flow.

4.4 Velocity Measurements of a Rotating Disk

To test the prototype DAV's velocity measuring capability, a wire attached to

a rotating disk was used to simulate a fluid particle in the flow. The maximum wire velocity obtainable with the rotating disk alone was about 15 m/s. In order to increase the measured speeds of the wire two things were done. The wire was taped to the end of an aerofoil shaped aluminum tube that was attached to the disk. In this way, the speed of the wire was increased due to the added distance between the center of the disk and the wire. Wire velocities obtained in this manner were between 20 and 42 m/s.

To simulate the effect of increasing the measured wire velocity further, the wire's image was magnified through the receiving optics. With a receiving lens magnification factor of 2, the speed of the wire's image (relative to the detector) was increased to 74 m/s.

4.4.1 Mean Velocity Measurements

Figure 38 is a plot of velocity measured with the prototype DAV vs. velocity calculated by a semi-independent method (see section **3.2**). Each value measured with the prototype represents an average of 1000 samples. The error bars on the graph result from the variation in the disk's angular velocity, which ranged from ± 0.05 Hz to ± 0.6 Hz from the set value. The straight line on the graph intersects the origin and has a slope equal to 1.

The measured velocity agrees with the calculated velocity to within 1% with only a few exceptions. At the calculated speed of about 15 m/s the error between

the velocity measured by the prototype and the calculated velocity is 2%. At the calculated speed of 30 m/s the error is 5%, and at the speed of 74 m/s the error is 4%. There are no definitive reasons for the increase in the error at those three measurement locations.

As the speed of a fluid particle increases, its image spends less time on the photodiodes. The ability of the prototype DAV to measure velocity depends on the ability of the primary amplifier to detect the current signals from the photodiodes. When the time required for the prototype DAV's analog signal to rise to the trigger level voltage becomes longer than the duration of the current signal from the photodiodes, then the prototype can no longer accurately determine the arrival time of a particle. Figure 38 shows that the prototype DAV is capable of accurately measuring mean velocity at flow speeds of greater than 60 m/s.

At such high velocities the prototype's resolution suffers greatly. A measured velocity of 65 m/s has an accuracy of ± 0.4 m/s. Increasing the clock speed driving the counters will increase the velocity resolution, but there is a limit to the maximum speed of the clock that can be used with the low power TTL circuitry ($\approx$ 25 MHz). Again, digitizing the analog signals could solve the resolution problem. An A/D board that could simultaneously sample both channels at 100 MHz would improve the prototype's resolution by two orders of magnitude at that same velocity (65 m/s).

4.4.2 Turbulence Intensity Measurements

A wire travelling through the measurement volume at a near constant rate shouldn't produce a noticeable fluctuating component of velocity. In actuality however, the effects of the signal noise produced by the prototype DAV coupled with the slight out of plane wobble of the disk create apparent velocity fluctuations. The slowly varying disk speed also affected the velocity fluctuations.

For a phenomenon with little or no turbulent fluctuations (such as the wire on the rotating disk), the measured value of $\overline{u'^2}$ can be shown to follow a theoretically derived function. The equation that the DAV uses to calculate velocity from the measured time of flight of a seed particle's image is

$$u = A/t \tag{1}$$

where u is the velocity component normal to the long axis of the bi-cell, t is the time of flight of a particle's image, and A is a constant equal to the distance travelled by the particle's image divided by the receiving lens magnification factor. Decomposing u and t into their mean plus fluctuating components, and performing a binomial expansion on the right hand side of equation (1) gives

$$\bar{u} + u' = \frac{A}{\bar{t}}(1 - t'/\bar{t} + (t'/\bar{t})^2 - \cdots). \tag{2}$$

After neglecting the second order and higher terms from equation (2), the mean velocity and the fluctuating velocity components can be separated giving

$$\bar{u} = \frac{A}{\bar{t}}, \quad u' = -A\frac{t'}{\bar{t}^2}. \tag{3}$$

If the velocity and time fluctuations are written as $\theta' = \theta'_a + \theta'_n$, where subscript 'a' refers to the actual value of the fluctuating component, and subscript 'n' refers to the fluctuating component due to the signal noise from the prototype DAV, then u' from equation (3) may be rewritten as

$$u'_a + u'_n = -\frac{A}{\bar{t}^2}(t'_a + t'_n). \tag{4}$$

After squaring and averaging both sides of equation (4) (the cross correlation terms from both sides drop out because there is no correlation between the 'noise' quantity and the 'actual' quantity), the equation appears as

$$\overline{u'^2_a} + \overline{u'^2_n} = \frac{A^2}{\bar{t}^4}\left(\overline{t'^2_a} + \overline{t'^2_n}\right). \tag{5}$$

$\overline{t'^2_n}$ is a constant defined by the peak-to-peak signal noise and the leading edge rise time of the signals. Because there is no correlation between the 'actual' velocity fluctuations and the 'noise' velocity fluctuations, equation (5) is equal to $\overline{u'^2}$. Combining equations (3) and (5), $\overline{u'^2}$ may be written as

$$\overline{u'^2} = a\bar{u}^4 + \overline{u'^2_a}. \tag{6}$$

a is a constant that is equal to $\overline{t'^2_n}/A^2$. For a phenomena with no turbulent fluctuations,

such as described above, equation (6) may be rewritten as

$$\overline{u'^2} \approx a\bar{u}^4 . \tag{7}$$

A plot of $\overline{u'^2}$ vs. u for the rotating disk measurements of Figure 38 is shown in Figure 39. The solid line on the graph represents the theoretical growth in $\overline{u'^2}$ according to equation (7). The constants a and b for the theoretical curve were calculated from a visual best fit of the form $\overline{u'^2} = a\bar{u}^4 + b$. The constant b was added to the equation so that the curve would fall between the data values.

The validity of the calculated value for a can be assured by comparing it to the derived results of section **4.1.1.** Velocity fluctuations due to noise for the prototype were found to be $\delta t = \pm 0.9\ \mu s$. δt is equal to twice the rms value of the fluctuations, or $\pm 2\sqrt{\overline{t'^2_n}}$. Therefore, according to the calculations of section **4.1.1** $\sqrt{\overline{t'^2_n}}$ is 0.45 μs. The constant a as defined in equation (6) is equal to $\overline{t'^2_n} / A^2$, which gives a value of 0.48 μs for $\sqrt{\overline{t'^2_n}}$.

The data for $\overline{u'^2}$ of Figure 39 closely follows the theoretical curve (the apparent scatter at low values of u is exaggerated due to the logarithmic scale) until the last four points are reached. These four data points were obtained with a magnification factor of greater than one. This necessitated a repositioning of the detector relative

to the receiving lens. It is possible that the detector could have been improperly aligned with respect to the receiving lens and resulted in this noticeable break from the theoretical for the last four data values.

4.5 Velocity Measurements in a Turbulent Wall Bounded Flow

Velocity measurements were made with both the prototype DAV and a hot-wire anemometer in a turbulent boundary layer with a freestream velocity of 10 m/s. The two sets of measurements, made in approximately the same location, are compared. The hot-wire was oriented normal to the mean flow. A cathetometer was used to place the hot-wire at its lowest position of 2.49 mm above the floor. The presence of the probe stem prevented the hot-wire from getting any closer to the wall. Thirty point measurements were taken with the hot-wire between 2.49 mm and 52.1 mm above the floor.

Measurements with the prototype DAV were made at 15 locations spanning the same range in the Y direction as the hot-wire data. Because of the excessive amount of scattered light from the laser beam, we were unable to take measurements closer than 2.49 mm to the wall. The location of the floor was found by intersecting the laser beam with the plexiglass at a very shallow angle ($< 2^{\circ}$). This created a streak of scattered light on the plexiglass floor. The streak of light was centered over the hot-wire profile location with an accuracy of ± 0.16 cm in the X direction and ± 0.64 cm in the Z direction.

The laser beam was then rotated about the lower mirror on the beam steering device into a horizontal position in preparation for making the velocity measurements. The angle through which the beam was rotated was measured with an accuracy of $\pm 0.005^{\circ}$ by measuring the vertical distance traversed by the beam at a location over 3 meters away. A dial indicator (with a resolution of 0.001 in.) was attached to a vertical extension of the laser table to measure the relative movement of the table in the Y direction with respect to the laboratory floor. There is an uncertainty of ± 0.14 mm in the Y location of the prototype DAV data.

The prototype DAV made velocity measurements at a rate of about 6.8 samples/sec. The main factors effecting the data rate are the flow seeding concentration, and the placement of the validation voltage levels. In validating only the 'good' signal pairs, approximately 19 of every 20 signals that reached the digital electronics were rejected. Increasing the data rate to 100 samples/sec would not be difficult to achieve. The laser power remained at 1.5 W during the profile. The receiving optics were situated with an elevation angle of 90° and an orientation angle of about 45°. The magnification factor was difficult to determine accurately prior to making the measurements, but it was near unity.

4.5.1 Mean Velocity Measurements

The raw data taken by the prototype DAV was first arranged into velocity histograms, from which the mean velocity and turbulence normal stress were extracted.

This data is plotted as probability density distributions for each measurement location in Figure 40. Each graph contains approximately 1000 samples.

Figure 41 is a plot of normalized velocity vs. height above the floor (in cm) for both the prototype and the hot-wire. The measurements with the prototype DAV were taken in a single traverse down from the initial point 52.1 mm above the floor. A trend in the prototype velocity data is quite noticeable. The profile starts out in good agreement with the hot-wire data and then worsens at each successive point, lagging further behind the hot-wire velocity values. The prototype's lagging error reaches a maximum of -7% at the center of the profile. At each point thereafter, the prototype's relative error decreases until the velocity measured by the prototype DAV exceeds the velocity measured by the hot-wire. By the last point in the profile, the relative error in the prototype DAV's measurement has reached a maximum of +9%.

The errors in the prototype DAV's mean velocity measurements are larger than the estimated errors discussed in sections **4.1** and **4.2**. The most likely explanation for the large amount of error is the slight relative movement that occurred between the laser table and the detector array as the table was traversed, and the large amount of stray laser light surrounding the core of the laser beam.

The mount that holds the detector (and all of the analog circuitry that is enclosed in the shielded box) tends to move with respect to the laser table when the table is moved. If this was happening during the profile taken with the prototype, then every time that the laser table was moved to the next point in the profile, the precision to

which the particle images were focussed onto the detector would become worse. Because of the prototype's sensitivity to the alignment of the detector, this would cause an error in its velocity measurements.

At the time these measurements were taken, the laser beam was surrounded by a significant amount of scattered laser light. The mask positioned around the sending beam (see Figure 13) only partially blocked the stray light. This stray light intersected the edge of the plexiglass floor when the core of the beam was 1.4 cm above the floor. The scattered laser light raised the dc voltage level of the analog signals. The amount of scattered light increased as the laser beam approached the floor, and the dc voltage level of the signals continued to rise. For the prototype to make reliable measurements, the ambient light level incident on the detector must remain constant during a profile.

4.5.2 Turbulence Intensity Measurements

$\overline{u'^2}$ was calculated from velocity histogram data for both the prototype DAV and the hot-wire measurements. The time averaged turbulence intensity normalized by the freestream velocity, $\sqrt{\overline{u'^2}}/u_{ref}$, was plotted against the vertical distance above the floor in Figure 42. The two plots show satisfactory agreement. The prototype data is within 1.5% in u_{ref} of the hot-wire data. Interestingly, the prototype data converges on the hot-wire values as the mean velocity of the flow decreases due to the presence of the floor. However, a reduction in the relative error between the two graphs only

occurs in the lower half of the profile. The two curves actually collapse near the floor, but then diverge again at the last two points. These results are consistent with the trends seen in the mean velocity profiles of Figure 41.

If it is assumed that the hot-wire anemometer measures the true turbulence intensity of the flow, then any difference between the hot-wire's values and those of the prototype would be due to some error caused by the prototype. If this error is mainly caused by the prototype DAV's signal noise, then the error could possibly be isolated and extracted from $\overline{u'^2}$. Starting with equation (5), the turbulence stress due to prototype noise is separated from the turbulence stress due to the velocity fluctuations. This is possible because the two are uncorrelated. If a measurement were taken in a part of the flow with exactly zero velocity fluctuations, then the turbulence stress measured would be entirely due to the signal noise. The equation for the fluctuations due to noise is

$$\overline{u'^2_n} = \frac{A^2}{\bar{t}^4}\overline{t'^2_n}. \tag{8}$$

If this equation is used at two different locations in the profile, a ratio of the two equations can be devised:

$$\left.\overline{u'^2_n}\right|_j = \left(\frac{\bar{u}_j^4}{\bar{u}_1^4}\right)\left.\overline{u'^2_n}\right|_1. \tag{9}$$

Equation (9) may be used to correct for the prototype error due to noise if the amount

of $\overline{u'^2}$ that is caused by the signal noise is known.

The difference between the turbulence stress measured by the prototype DAV and the turbulence stress measured by the hot-wire at the first point in the profile of Figure 42 was chosen to equal the error due to the prototype DAV. The reason for choosing the error value from the first point in the profile, is because at that location the alignment of the receiving optics should have been at its best since the laser table had not been moved prior to that measurement. Applying the correction to the data for the prototype DAV, the two curves now appear as in Figure 43. The prototype's turbulence value at the first point in the profile has of course collapsed exactly onto the hot-wire's value. Except for two locations, the rest of the data shows only a slight improvement. The prototype DAV data now lies within about 1% in u_{ref} of the hot-wire data.

The value of $\overline{u'^2_n}$ that was chosen to represent the error due to prototype noise for the 'corrected' data of Figure 43, leads to a value for $\overline{t'^2_n}$ that is an order of magnitude larger than the value that was calculated empirically in section **4.4**. The apparent error in $\overline{u'^2}$ due to the prototype (which is graphically represented by the gap between the two curves of Figure 42) is eight times greater than the error caused by the signal noise alone. Obviously, most of the error in the prototype DAV's turbulence stress comes from all of the other sources that were discussed in sections **4.1**, **4.2**, and **4.5.1**.

5.0 Conclusions

The prototype DAV, a novel, proof-of-concept laser velocimeter, was developed and subsequently tested. The prototype DAV is capable of making one component velocity measurements in flows of up to 60 m/s.

The conclusions from this work are as follows:

1. The DAV is a viable concept for measuring mean velocity and turbulence intensity.

2. The current-to-voltage converter in the primary stage is responsible for all of the prototype DAV's dynamic response. The amount of signal gain required must be balanced against the amount of signal bandwidth desired and the amount of noise that can be tolerated.

3. High quality receiving optics are absolutely necessary for the prototype DAV to make accurate velocity measurements.

4. The main factors that contribute to the inaccuracy of the prototype are the signal noise and the signal rise time. The prototype DAV's velocity resolution is controlled solely by the speed of the clock that drives the binary counters.

5. The size and shape of the measurement volume is governed by the size of the detector array, the diameter of the laser beam, and the characteristics of the receiving optics.

6. The effects of image magnification upon the prototype DAV's characteristics are widespread. Magnification decreases the size of the measurement volume but also reduces the velocity resolution. Focusing the sending beam can also reduce the sized of the measurement volume, and increase the prototype's signal-to-noise ratio.

7. The maximum measurable image velocity (relative to the detector) of the prototype DAV is limited by the frequency response and the speed of the free running clock.

8. An unknown phenomena causes 'spikes' to appear on the voltage signals which can result in errors in the measurement of mean velocity.

9. The prototype is accurate to within 10% in measuring mean velocity.

Bibliography

Adamczyk, A. A. and Rimai, L. 1980, "2-Dimensional particle tracking velocimetry (PTV): technique and image processing algorithms", *Experiments in Fluids*, Springer-Verlag, Berlin, Germany, vol. 6, pp. 373-380.

Blackwelder, R. F. 1981, "Hot-wire and hot-film anemometers", *Methods of experimental physics: fluid dynamics*, Academic Press, New York, NY, vol. 18, part A, pp. 259-314.

Boutier, A. and Lefevre, J. 1988, "Mosaic laser velocimetry", *4th International Symposium on Appl. of Laser Anem. to Fl. Mech.*, Lisbon, Portugal, July 11-14, Springer-Verlag, Berlin, Germany.

Buckingham, M. J. 1983, Noise in electronic devices and systems, Ellis Horwood Limited, Chichester, England.

Burr-Brown, 1987, "Photodiode monitoring with op-amps", The handbook of linear IC applications, Burr-Brown Inc., pp. 192-201.

Burr-Brown, 1989, Integrated circuits data book, Burr-Brown Inc.

Chesnakas, C. J., Andrew, P. L., and Ng, W. F. 1991, "An evaluation of particle lag prediction techniques in supersonic flows", *Yokohama Int. Gas Turbine Congress*, Yokohama, Japan, October 27-November 1.

Cho, Y. C. 1989, "Digital Image velocimetry", *Applied Optics*, Optical Society of America, Inc., Washington, D.C., vol. 28, February 15, pp. 740-748.

Devenport, W. J., Evans, G. P., and Sutton, E. P. 1990, "A traversing pulsed-wire probe for velocity measurements near a wall", *Experiments in Fluids*, Springer-Verlag, Berlin, Germany, vol. 8, pp. 336-342.

Dowling, D. R., Lang, D. B., and Dimotakis, P. E. 1989, "An improved laser-Rayleigh scattering photodetection system", *Experiments in Fluids*, Springer-Verlag, vol. 7, pp. 435-440.

Dudderar, T. D. and Simpkins, P. G. 1987, "Summary of a talk on two-dimensional fluid velocity measurement by laser speckle velocimetry", *AIAA 19th Fluid Dynamics, Plasma Dynamics and Lasers Conference*, AIAA-87-1375, Honolulu, Hawaii, June 8-10, AIAA, New York, NY.

Durst, F., Melling A., and Whitelaw J. H. 1976, Principles and practice of laser-Doppler anemometry, Academic Press Inc., London, England.

Flugge, H. 1983, "Laser-dual-focus system for measuring the flow through narrow rod bundles", *Experiments in Fluids*, Springer-Verlag, Berlin, Germany, vol. 1, pp. 37-41.

Hirleman, E. D., Yue, Y., Berman, N. S., and Guan, D. X. 1984, "Single beam laser velocimetry (L1V) in turbulent flows", *2nd International Symposium on Appl. of Laser Anem. to Fl. Mech.*, Lisbon, Portugal, July 2-5, Ladoan Inc., Portugal.

Horrowitz, P. and Hill, W. 1989, The Art of Electronics, Cambridge University Press, Cambridge, England.

Kline, S. J. and McClintock, F. A. 1953, "Describing uncertainties in single sample experiments", *Mechanical Engineering*, American Society of Mechanical Engineers, New York, NY, vol. 75, pp. 3-8.

Lancaster, D. 1974, TTL cookbook, Horwood W. Sams & Co. Inc., Indianapolis, Indiana.

Naqwi, A. and Durst, F. 1989, "Computation of light scattering from a dual-beam system", Lehrstuhl für Strömungsmechanik, University of Erlangen, Germany.

Ott, H. W. 1976, Noise reduction techniques in electronic systems, John Wiley & Sons, New York, NY.

Saripalli, K. R. and Simpson, R. L. 1980, "Investigation of blown boundary layers with an improved wall jet system", NASA contractor report 3340.

Silicon Detector Corporation, 1984, Product data sheet, 400-44-007.

Smith, E. J., Rife, M. C., and Devenport, W. J. 1990, "Investigation of the small boundary layer tunnel", AOE department, VPI, Report VPI-AOE-175.

Smith, J. I. 1971, Modern operational circuit design, John Wiley & Sons, New York, NY.

Wong, Y. J. 1976, Function circuits - design and application, McGraw-Hill, New York, NY.

Figures

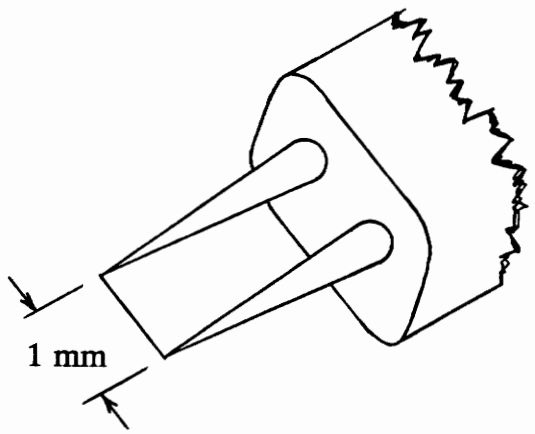

Figure 1 A single sensor hot-wire anemometer

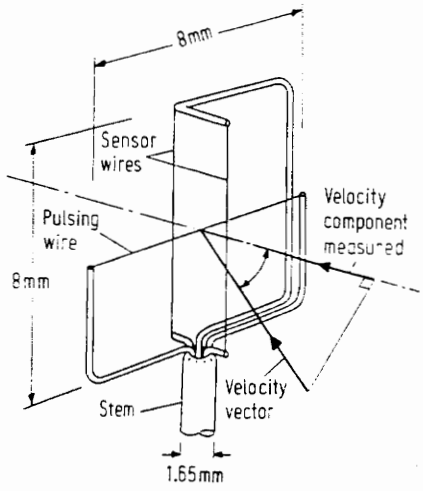

Figure 2 A standard pulsed-wire probe (Devenport, *et al.*, 1990)

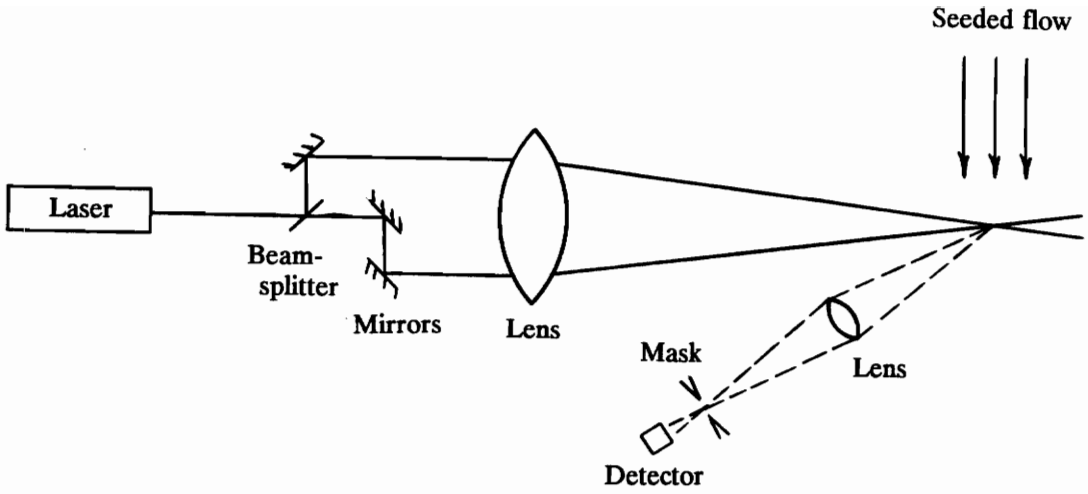

Figure 3 A dual-beam type laser-Doppler anemometer with receiving optics in the back-scatter mode

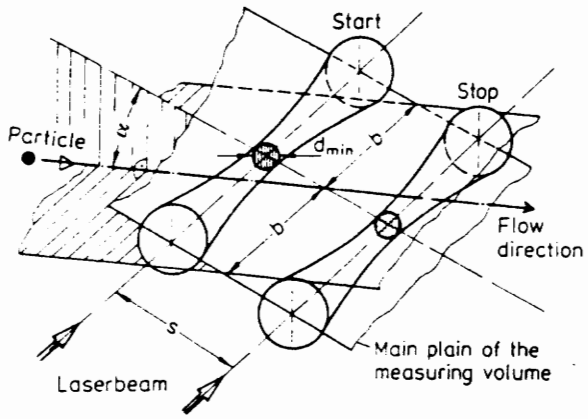

Figure 4 An L2F measurement volume geometry showing 'start' and 'stop' beams (Flugge, 1983)

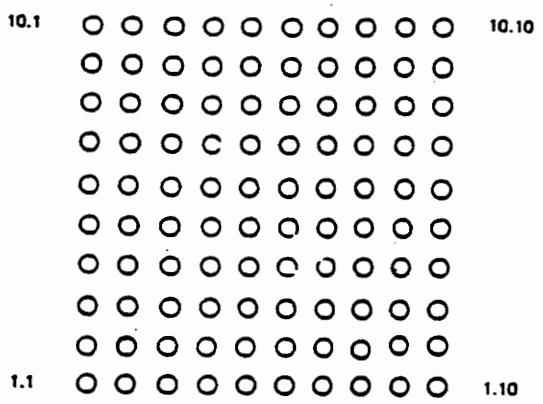

a) 100 optical fibers arranged into a 10×10 grid make up the detector

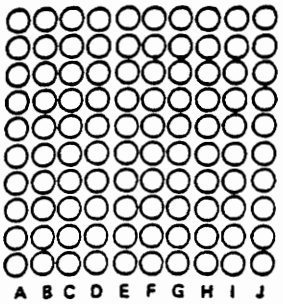

b) Each row of fibers is an active trigger

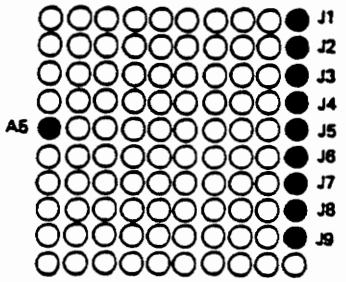

c) A5 acts as a 'start' signal; J1-J9 act as 'stop' signals

Figure 5 (a) The 10×10 mosaic detector for mosaic laser velocimetry; different operating configurations: (b) dash mode, (c) L2F mode (Cho, 1989)

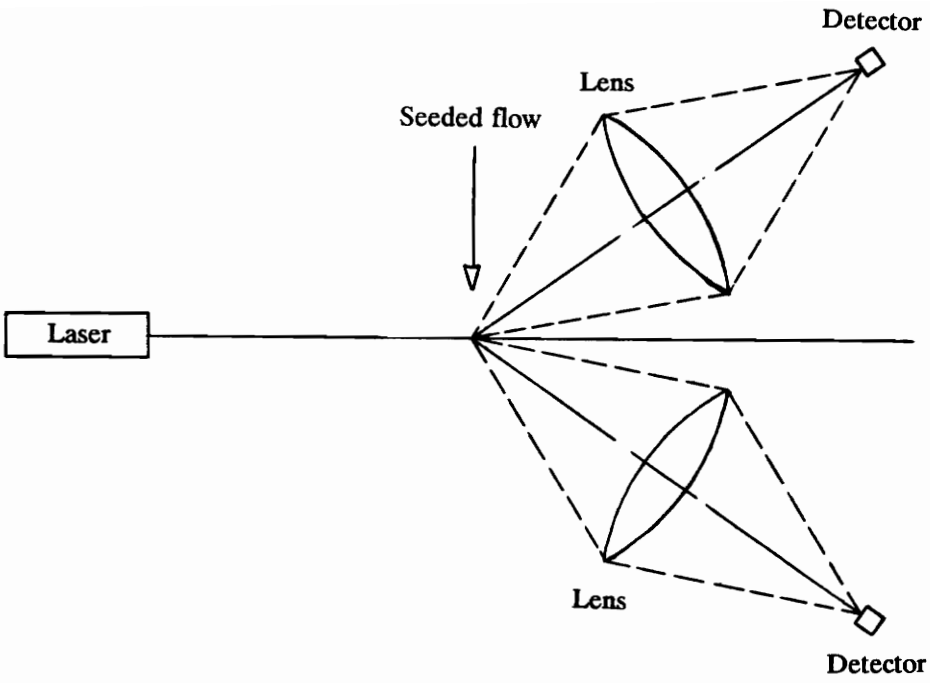

Figure 6 A typical setup for measuring one, two, or three velocity components with the DAV

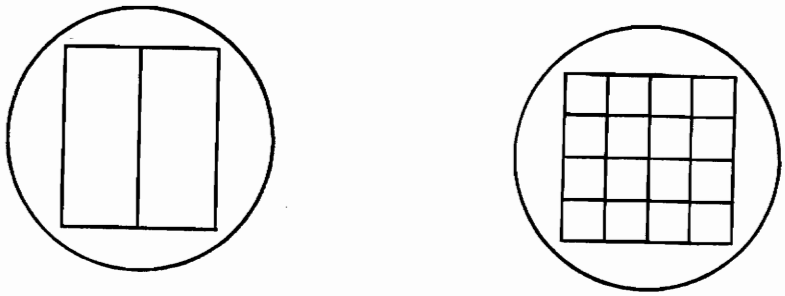

a) 2 element array

b) 16 element array

Figure 7 PIN photodiode detector arrays for the DAV: (a) 1-D detector array, (b) 2-D detector array

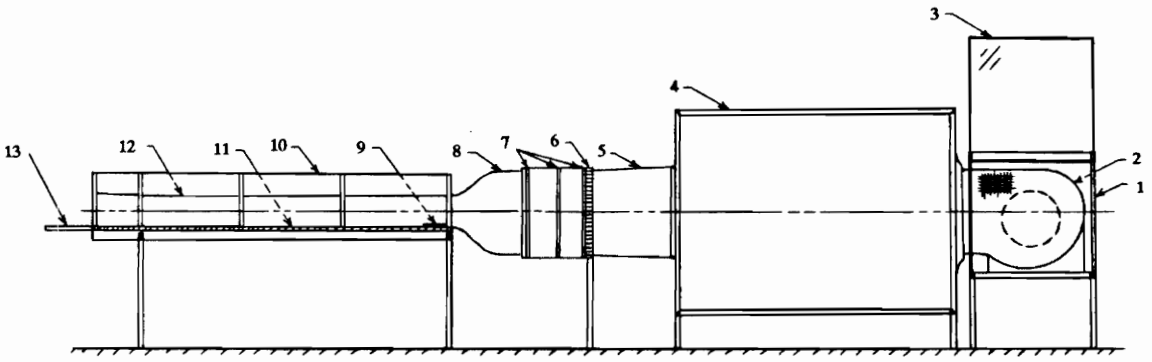

1. Filter box
2. Blower
3. Damper
4. Plenum
5. Contraction
6. Honeycomb
7. Screens
8. Contraction
9. Roughness element
10. Glass side walls
11. Bottom wall
12. Top wall
13. Plexiglass extension

Figure 8 The open circuit wind tunnel used to test the prototype DAV

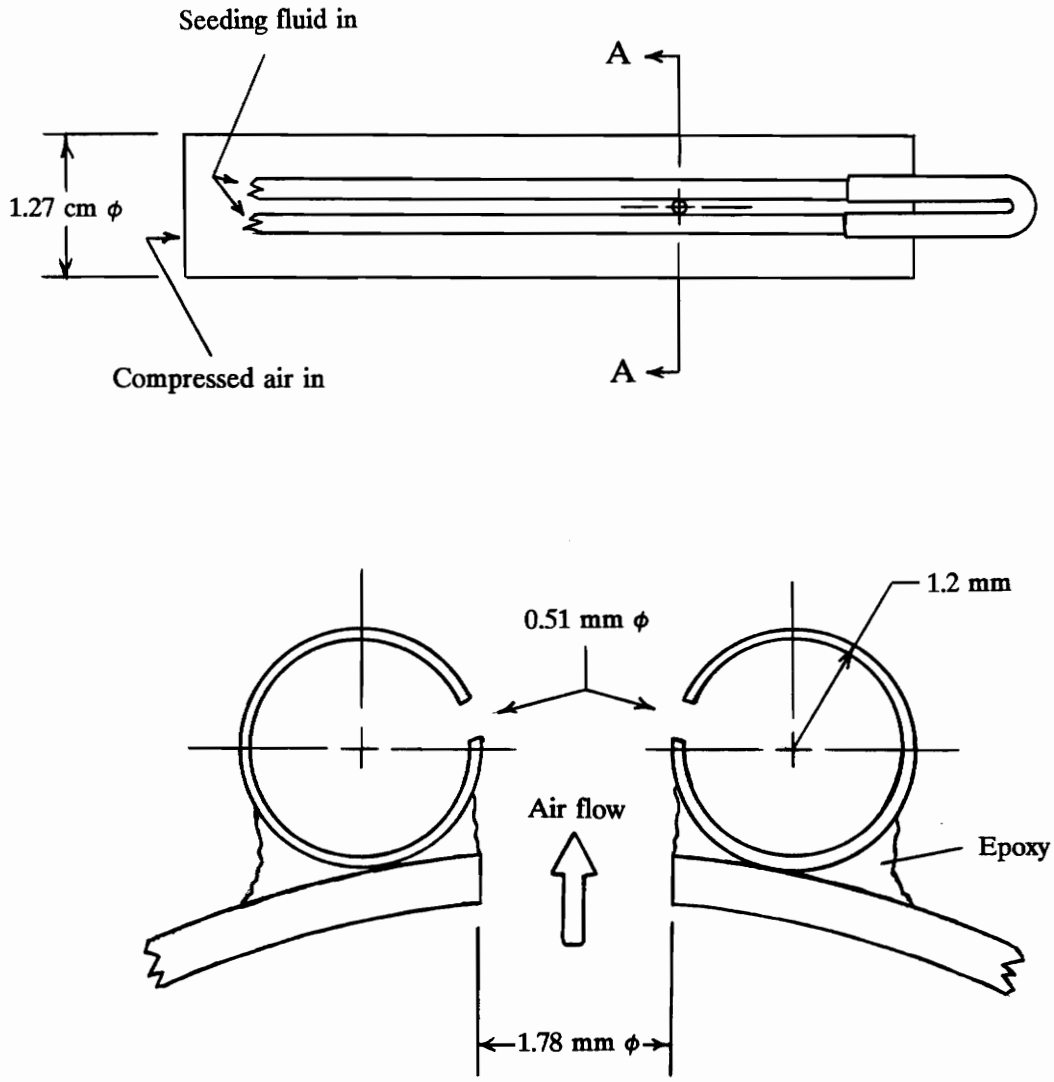

Figure 9 The seeder for the wind tunnel (note: drawings are not to scale)

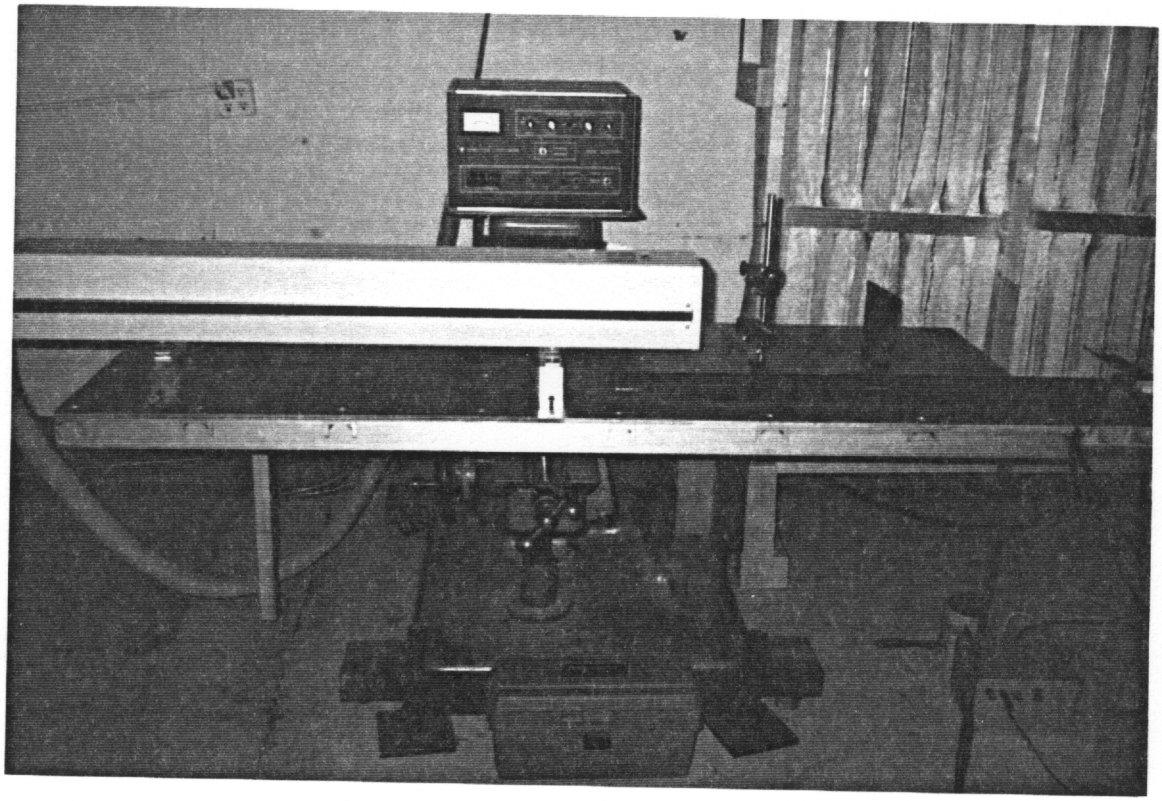

Figure 10 Photograph of laser table mounted to a milling machine traverse; also shown are the laser, beam steerer, and mask attached to an optical rail

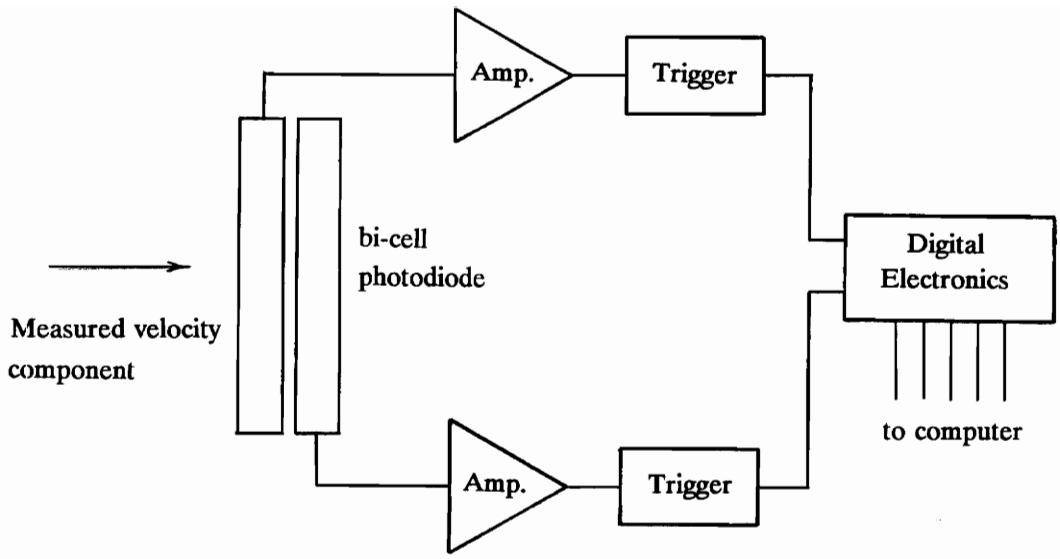

Figure 11 A schematic representation of the prototype DAV's circuitry with the bi-cell photodiode detector (not to scale)

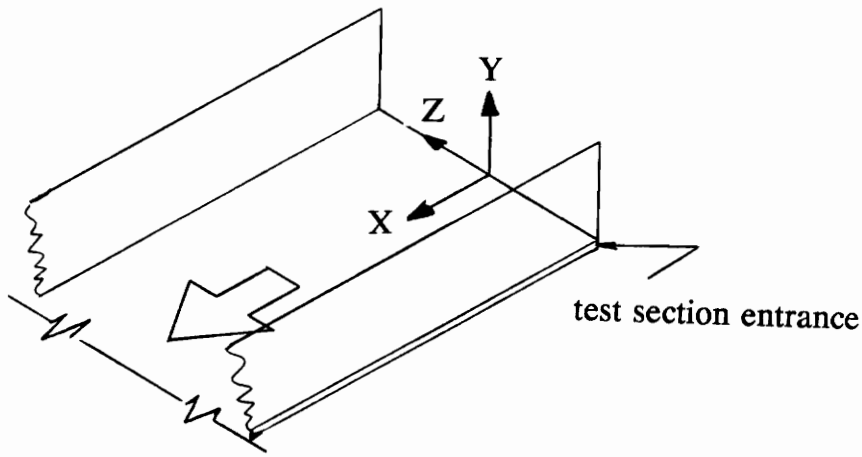

Figure 12 The co-ordinate system

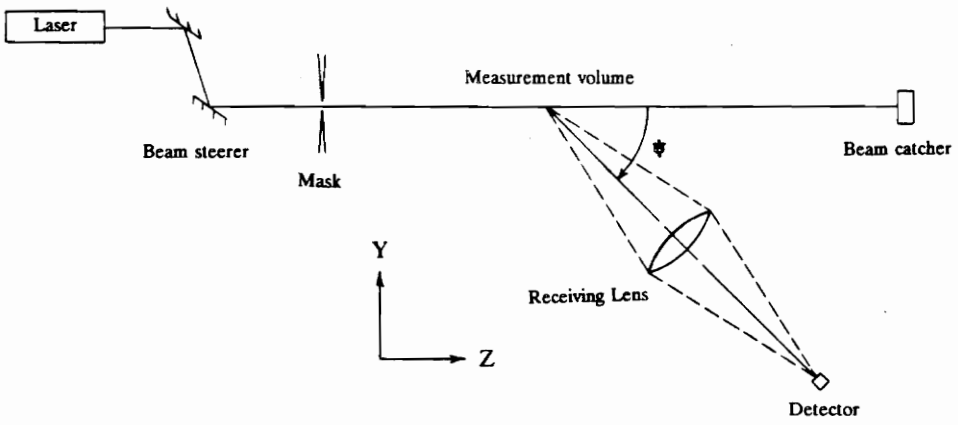

Figure 13 The optical layout for the prototype DAV; flow travels into the paper

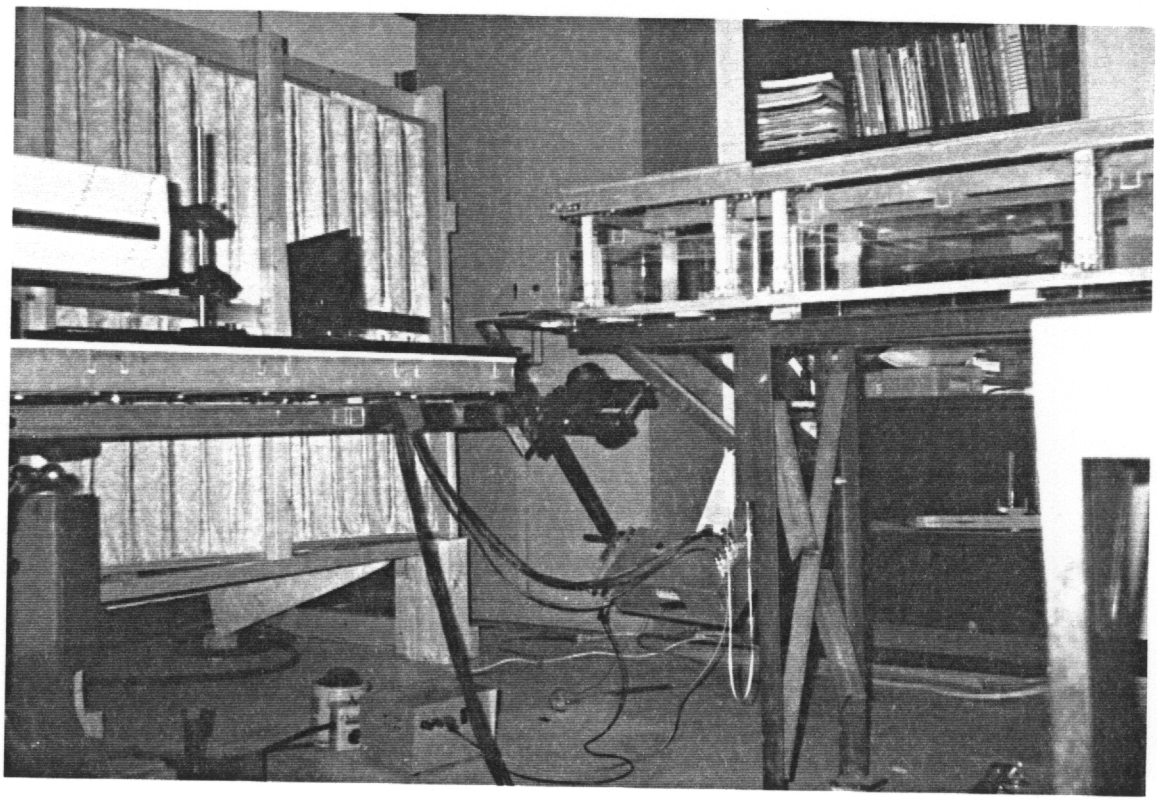

Figure 14 The receiving lens and the detector mounted to the laser table

SD160-24-21-021 bi-cell photodiode

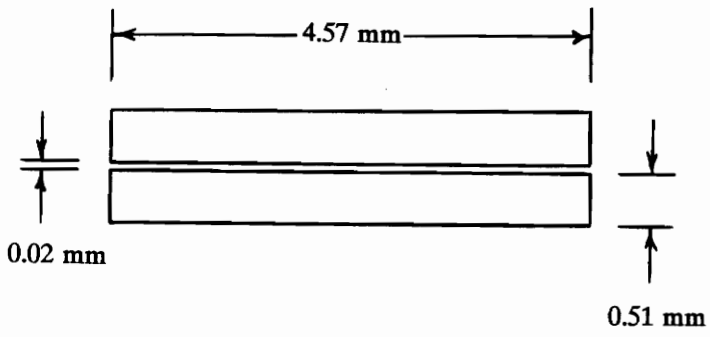

Figure 15 The bi-cell PIN photodiode used for the detector with the prototype DAV; the gap between the diodes is not to scale (Silicon Detector Corp., 1984)

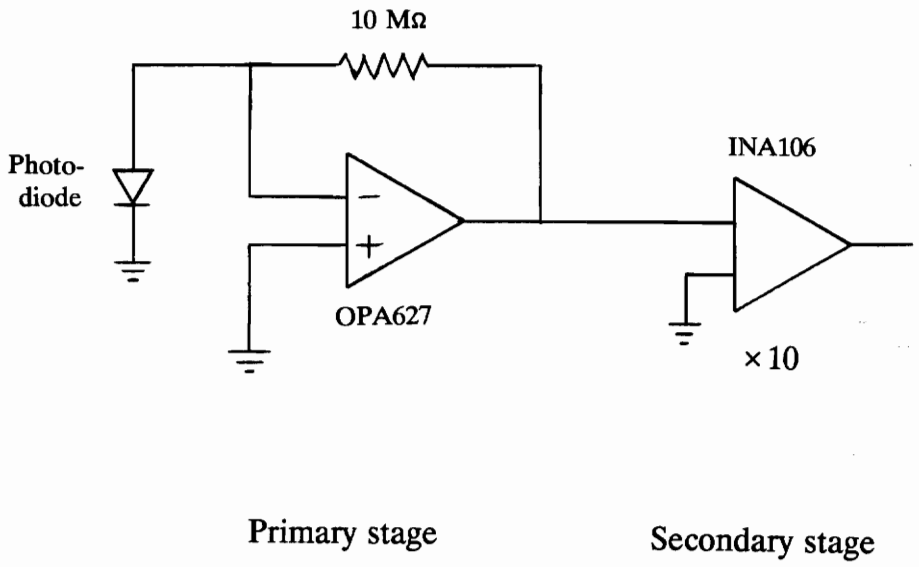

Figure 16 The amplification circuitry for one channel of the prototype DAV

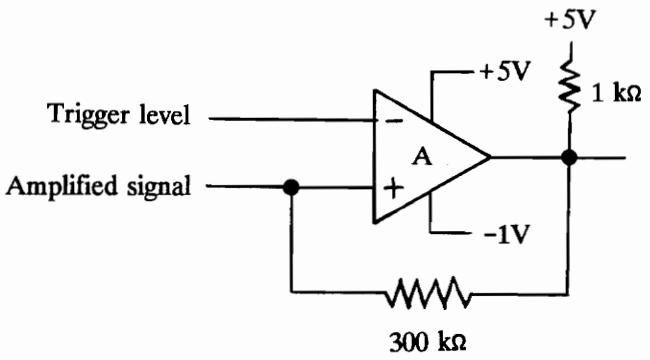

A. ¼LM339

Figure 17 Non-inverting Schmidt trigger circuit

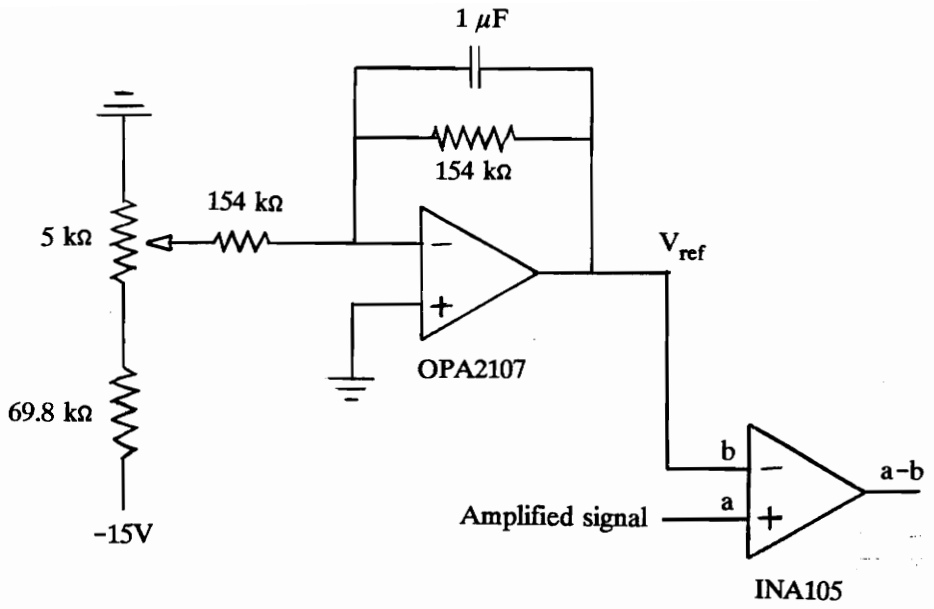

Figure 18 Pre-conditioning circuit for the trigger level voltage and the amplified signal

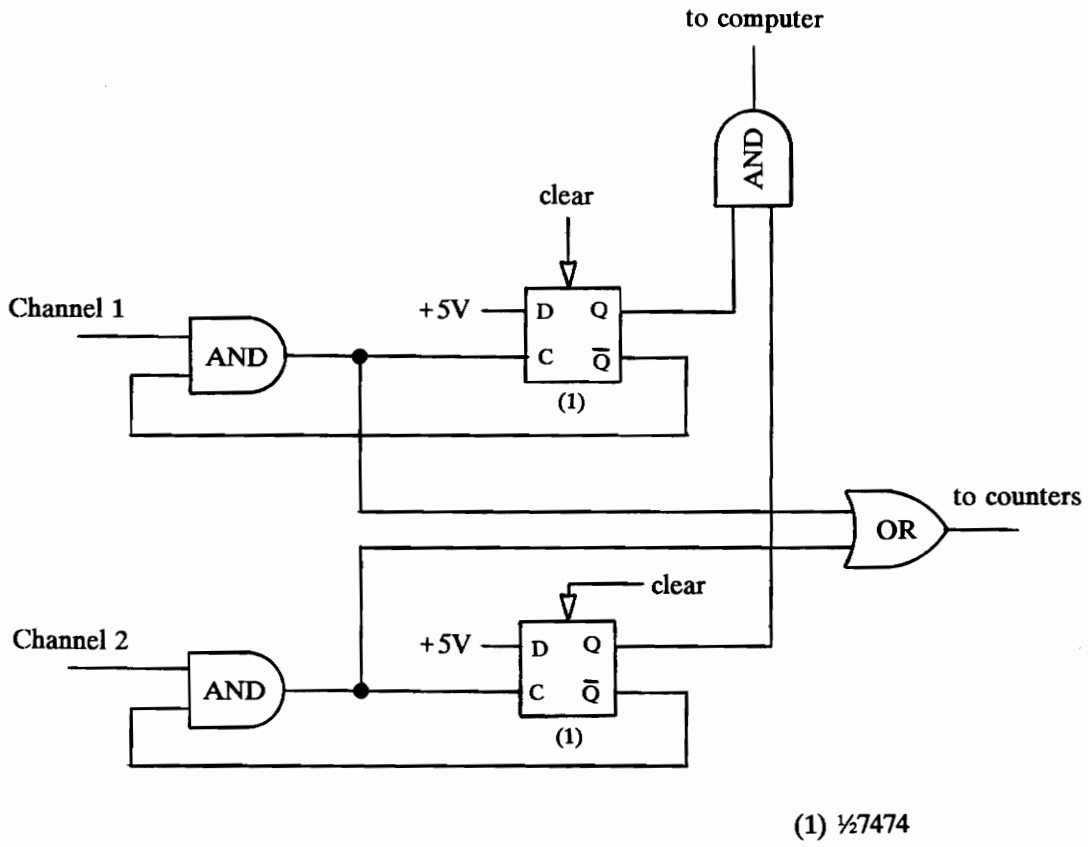

Figure 19 Digital timing circuit for prototype DAV

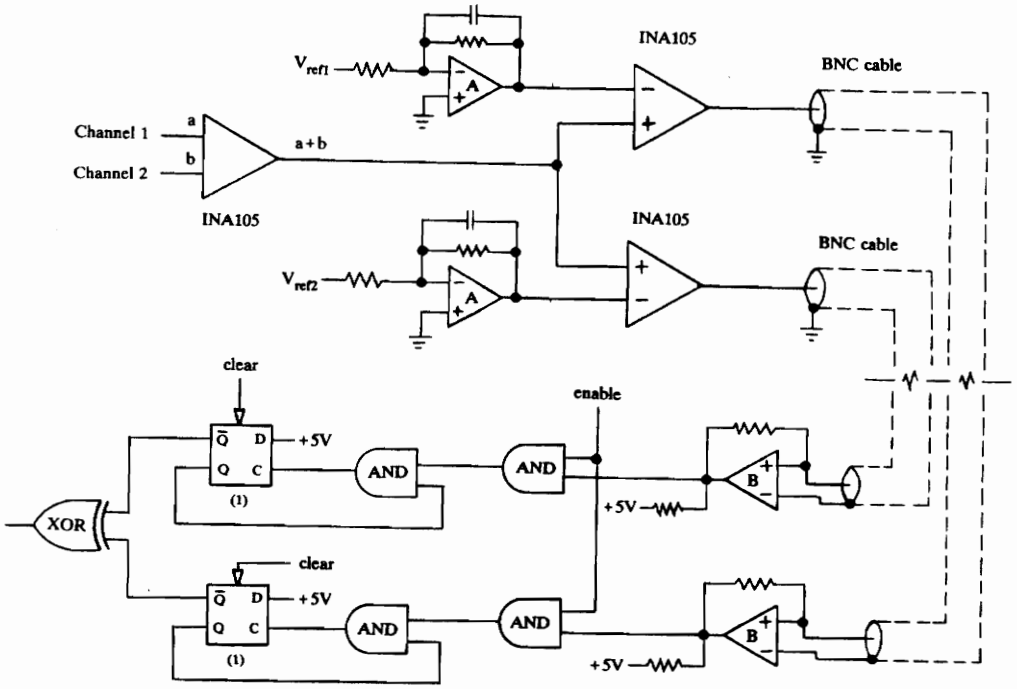

A. OPA2107 B. ¼LM339 (1) ½7474

Figure 20 The validation circuit; the two halves of the circuit (separated by the BNC cables) are powered from different voltage supplies

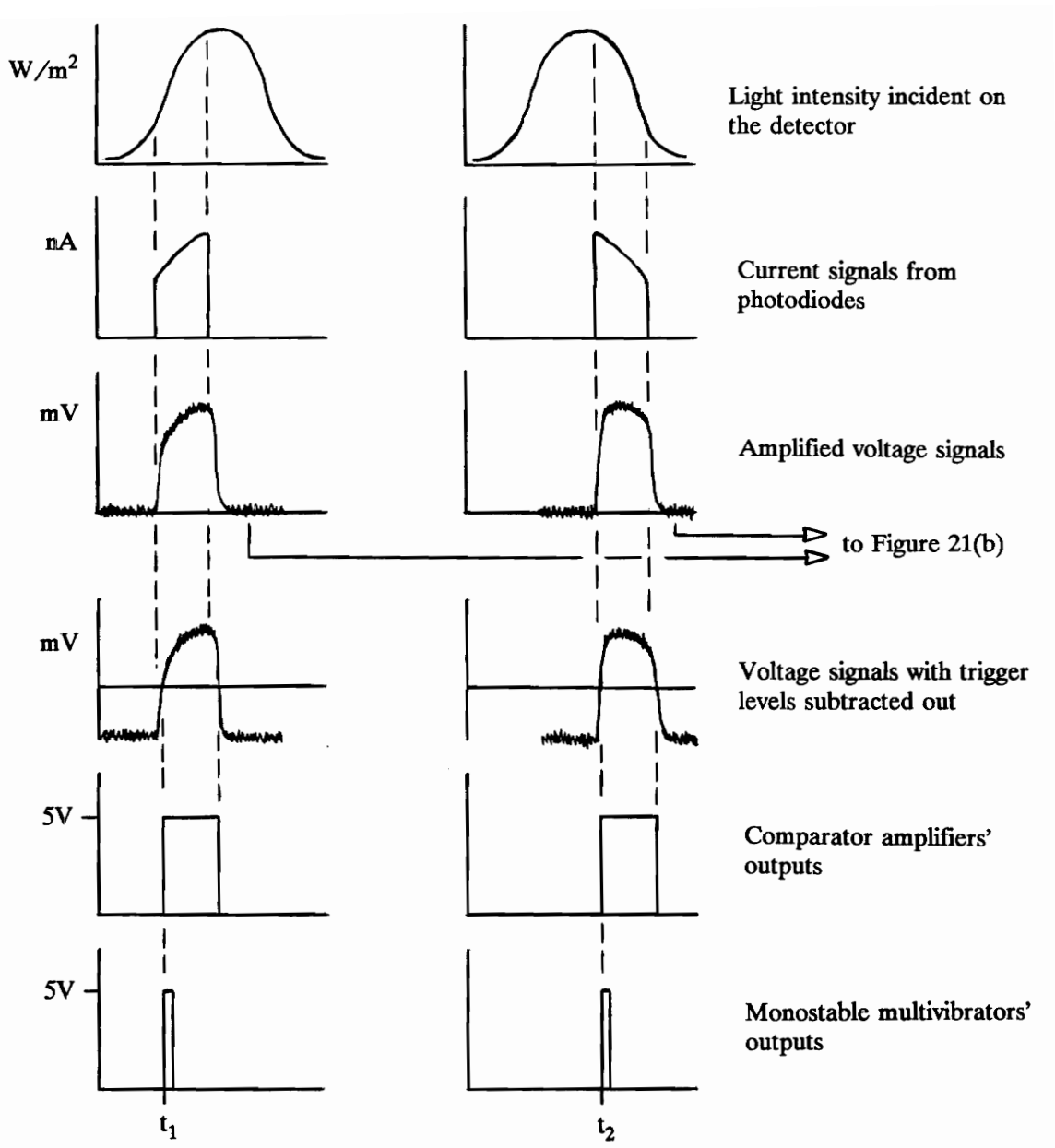

Figure 21 The steps involved in processing the optical signals produced by a particle's image as it crosses over the detector array: (a) the analog and digital circuitry; t_2-t_1 is the time of flight of a particle

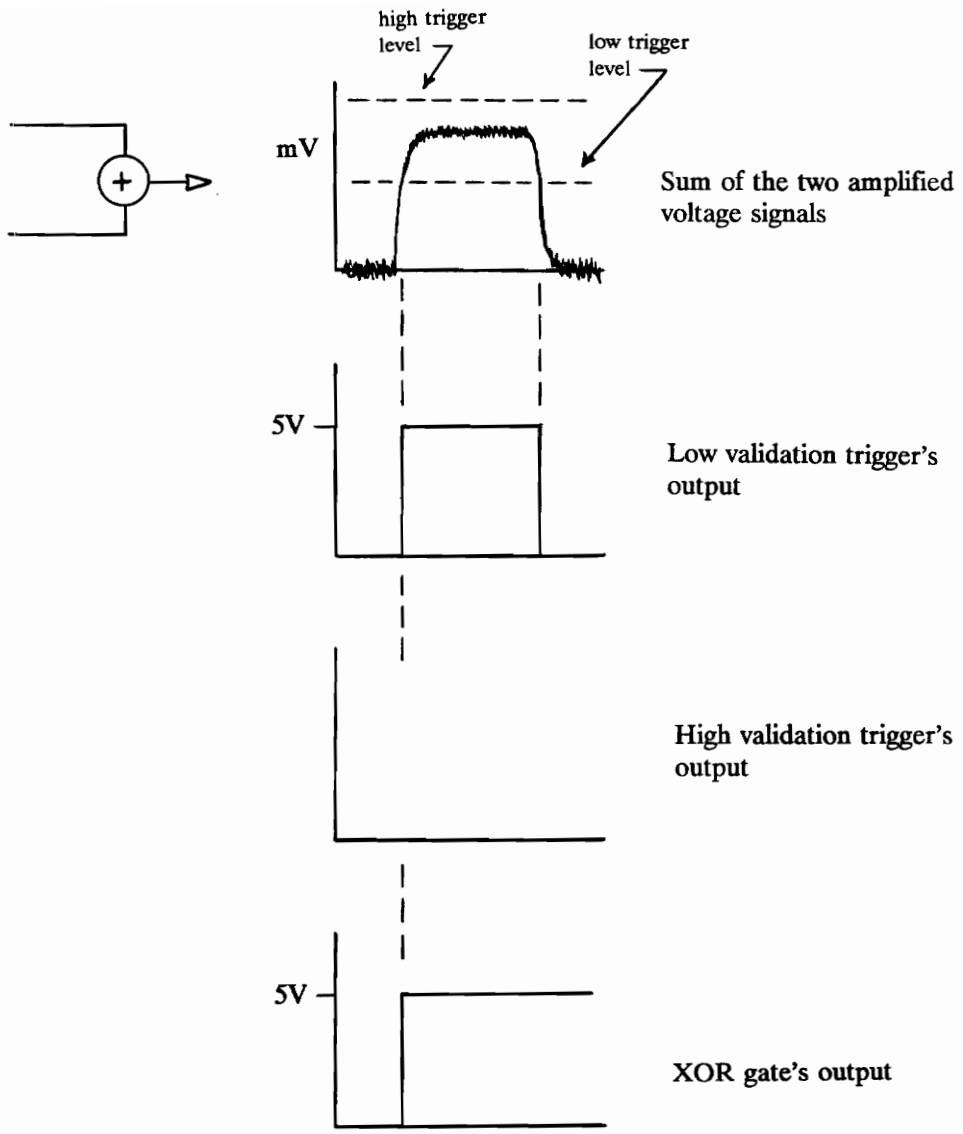

Figure 21 (continued) (b) the validation circuitry; output for a 'good' signal pair

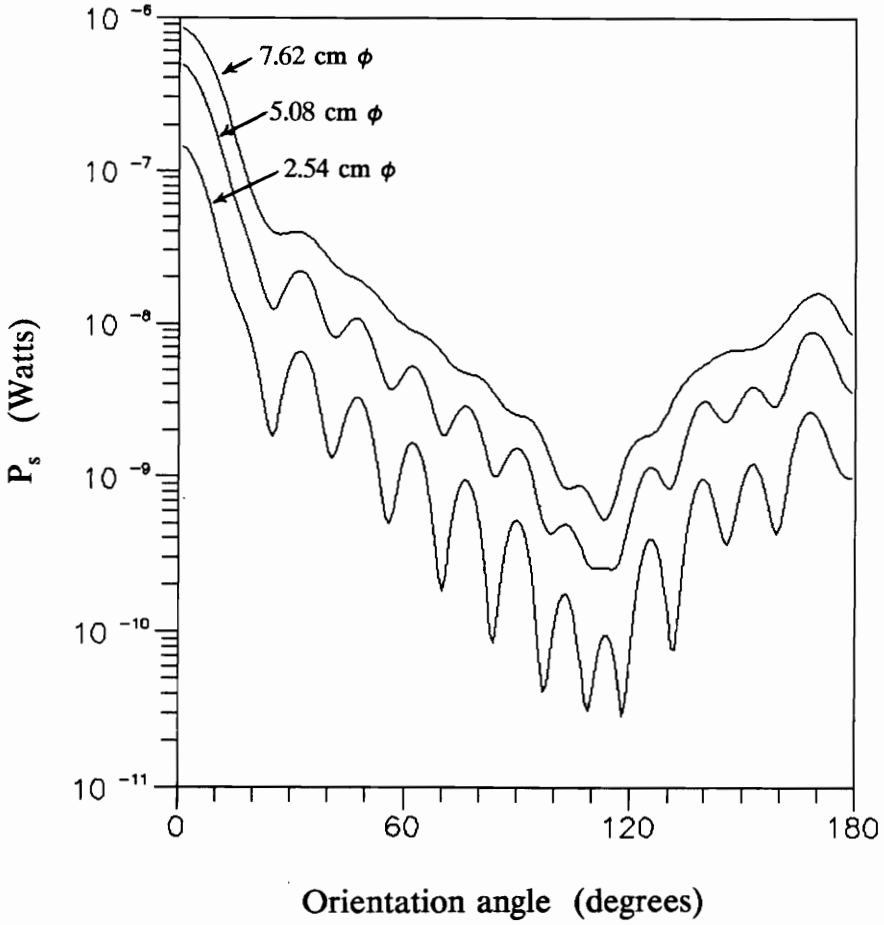

Figure 22 Scattered light power vs. orientation angle for receiving lens diameters of 2.54, 5.08, and 7.62 cm; calculated by the computer program STREU (Naqwi and Durst, 1989)

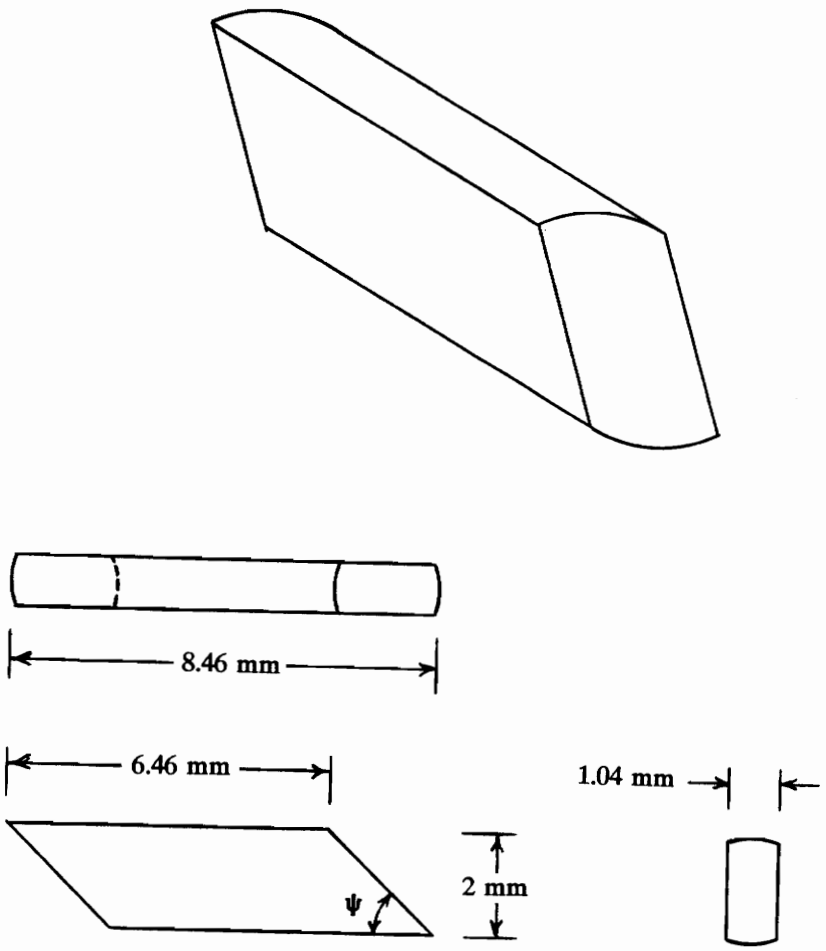

Figure 23 Measurement volume geometry for the prototype DAV; dimensions are for $\psi = 45^{\circ}$; 3 view drawing is to scale

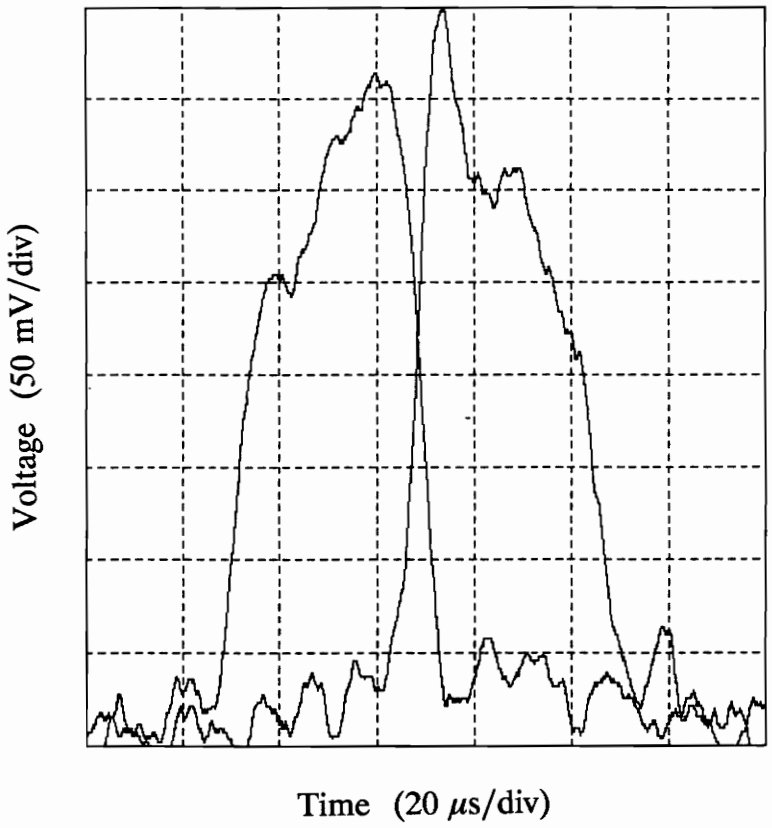

Figure 24 Amplified voltage signals generated by the prototype DAV measuring the speed of a rotating disk using the camera lens for the receiving lens

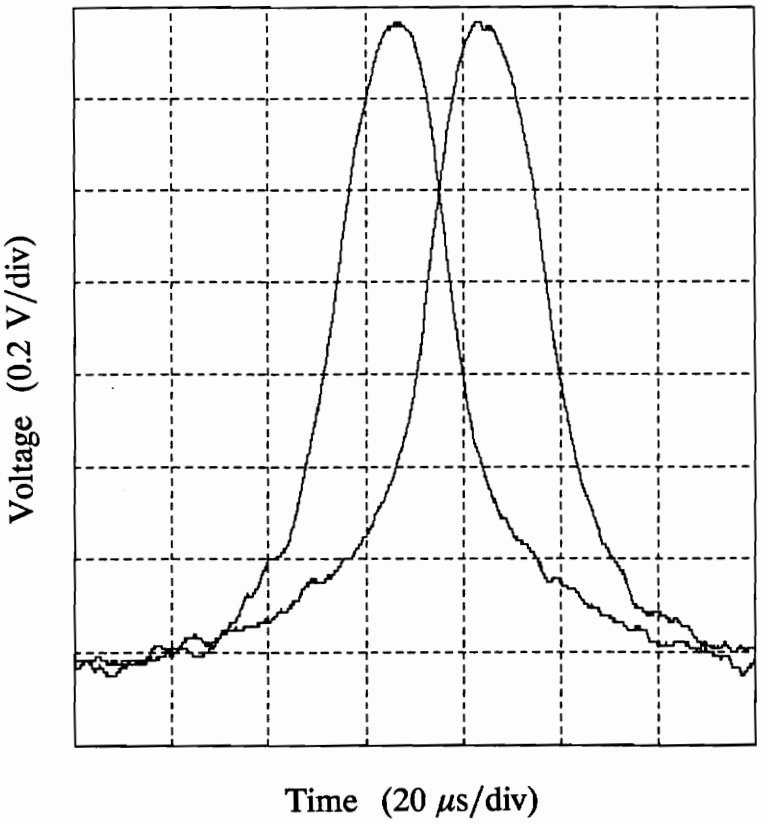

Figure 25 Amplified voltage signals generated by the prototype DAV measuring the speed of a rotating disk using a compound receiving lens

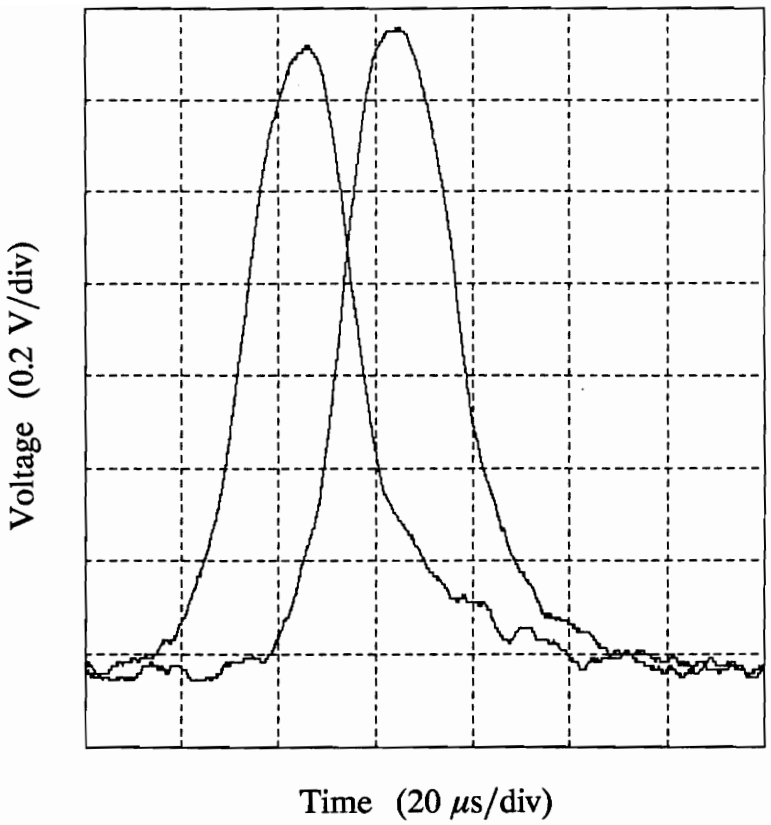

Figure 26 Amplified voltage signals generated by the prototype DAV measuring the speed of a rotating disk using a masked compound receiving lens

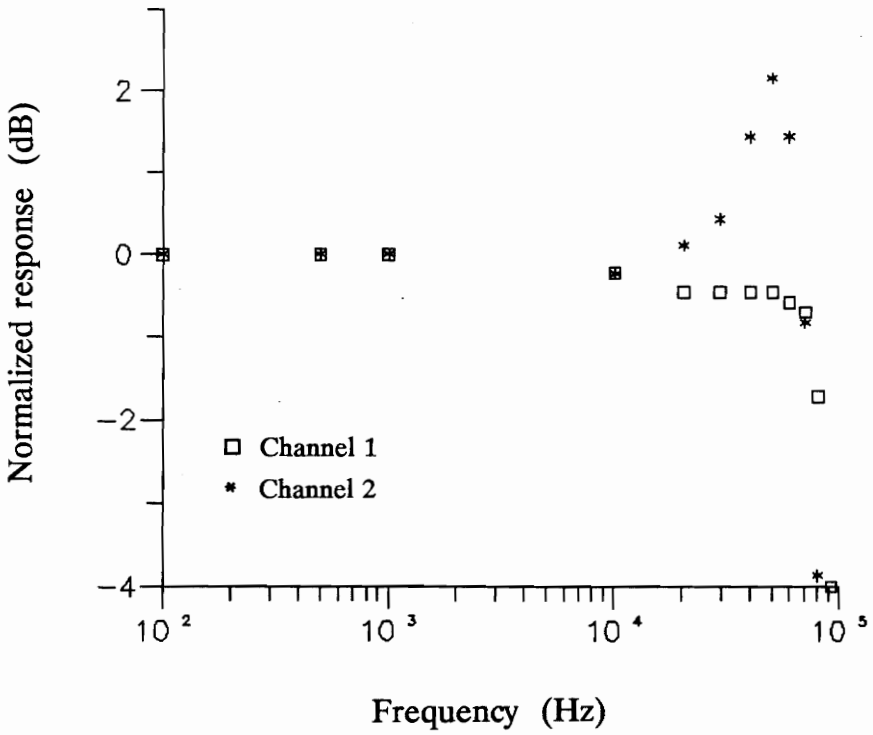

Figure 27 Frequency response of both channels of the amplification circuitry for the prototype DAV

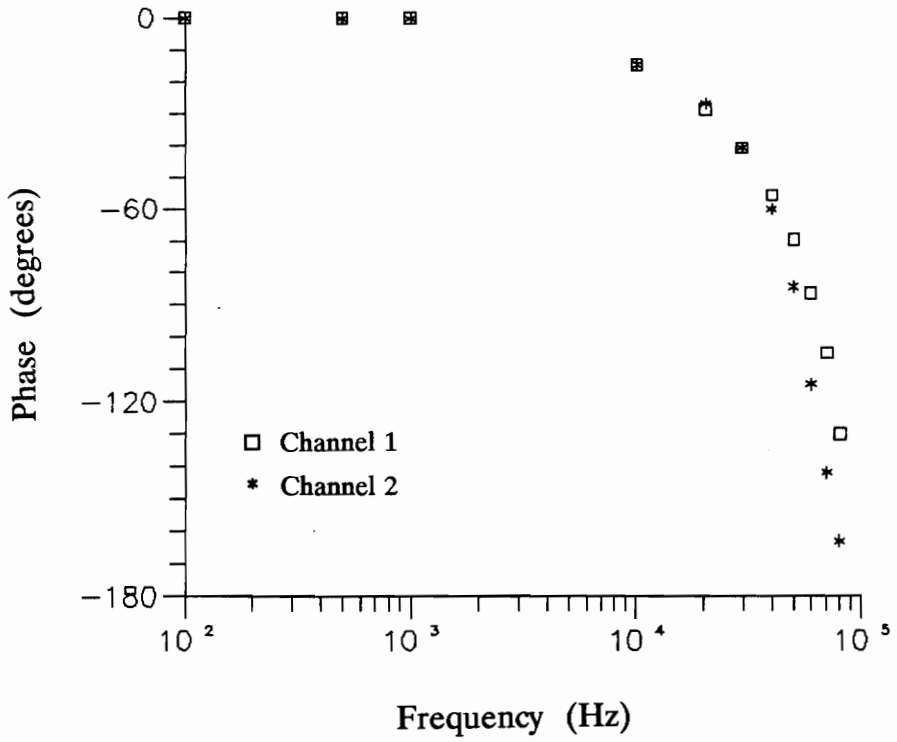

Figure 28 Phase response of both channels of the amplification circuitry for the prototype DAV

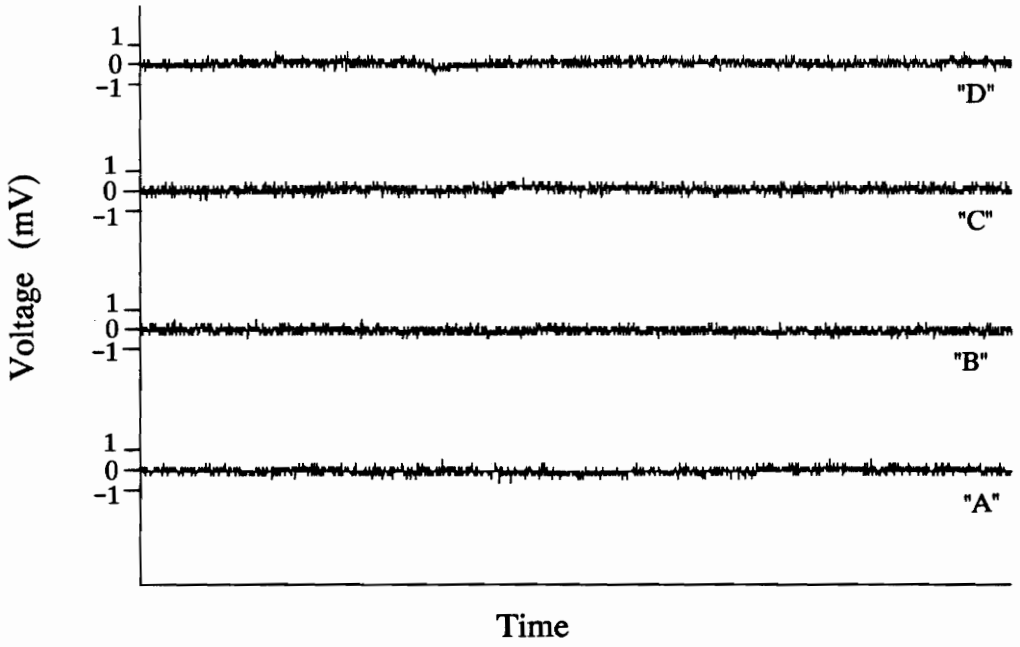

"A" : Two power supplies connected in parallel; an HP 6200B and an HP 6216C

"B" : Power One (HBAA-40W-A)

"C" : Condor (HBB15-1.5-A)

"D" : Power One (CP131)

Figure 29 Power supply noise for four different power supplies

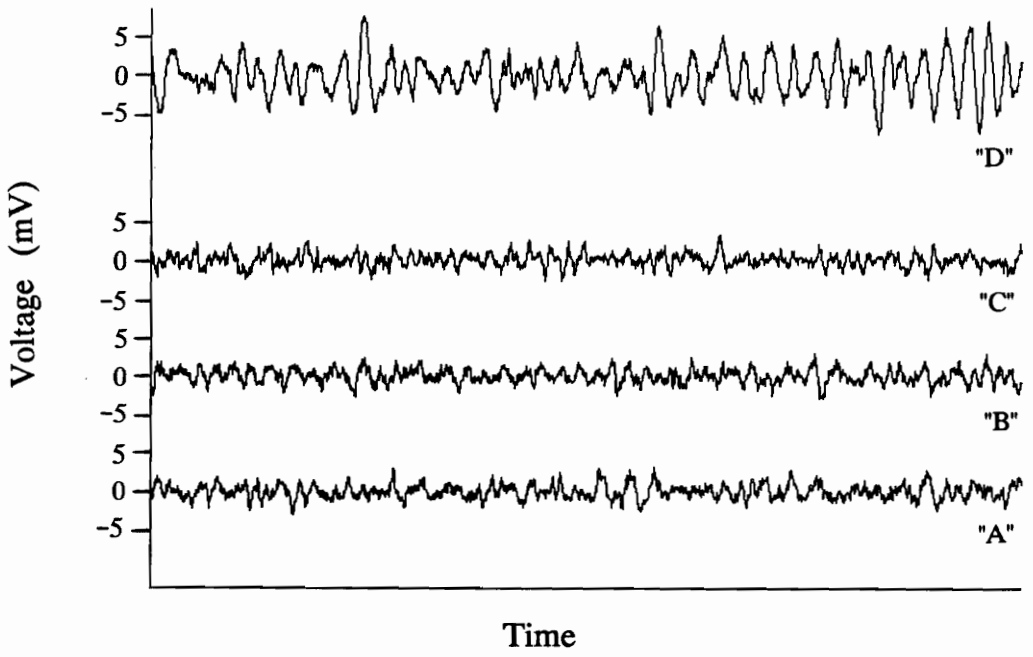

"A" : Two power supplies connected in parallel; an HP 6200B and an HP 6216C

"B" : Power One (HBAA-40W-A)

"C" : Condor (HBB15-1.5-A)

"D" : Power One (CP131)

Figure 30 Output prototype signal noise due to four different power supplies (same power supplies of Figure 29)

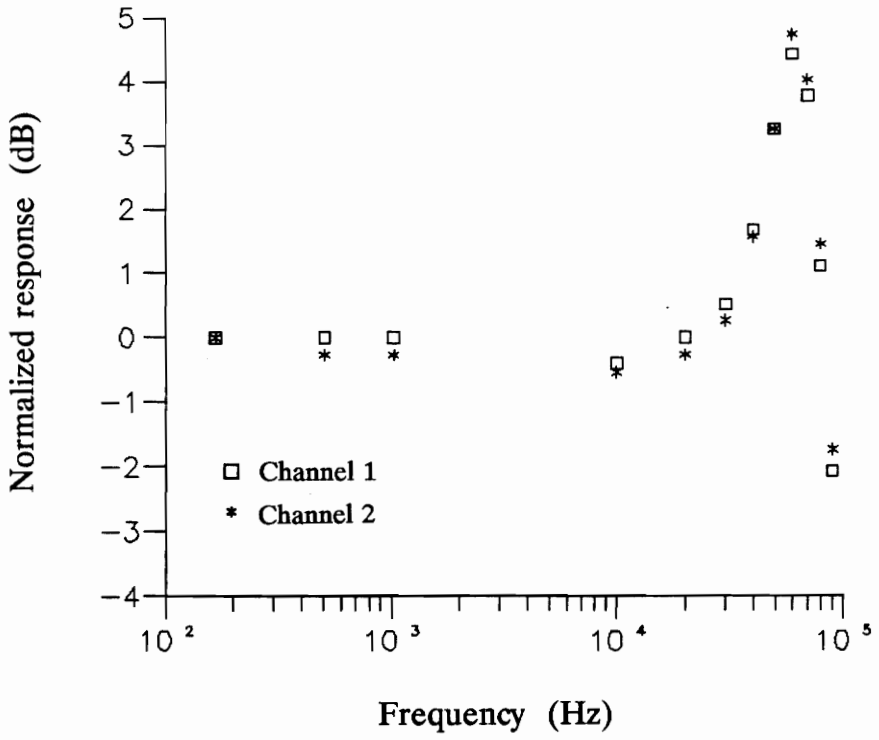

Figure 31 Effect of signal gain peaking on the amplification circuit's frequency response

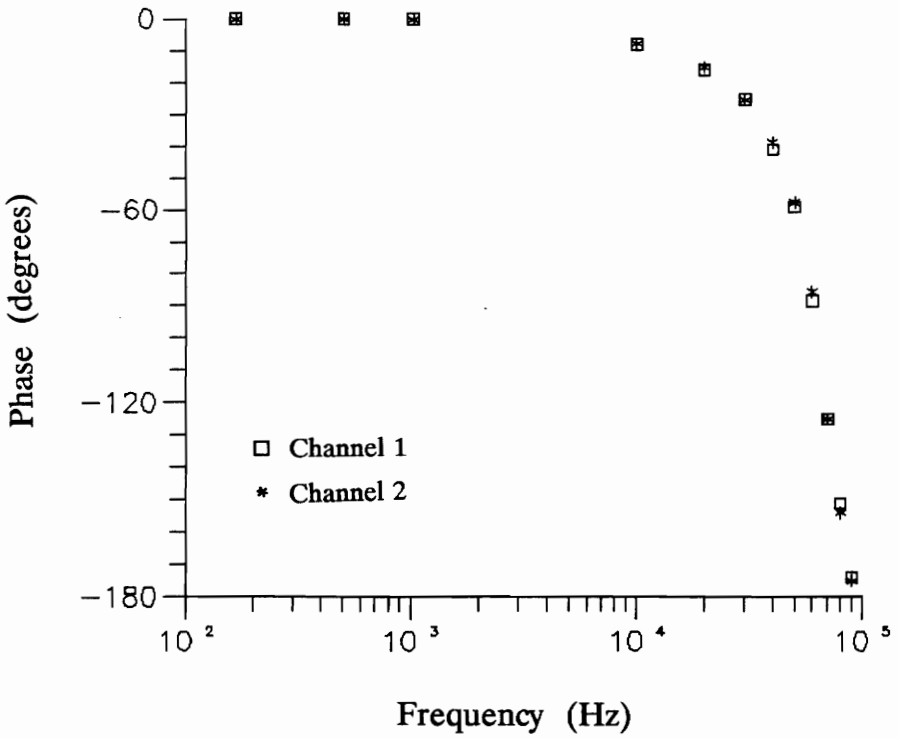

Figure 32 Effect of signal gain peaking on the amplification circuit's phase response

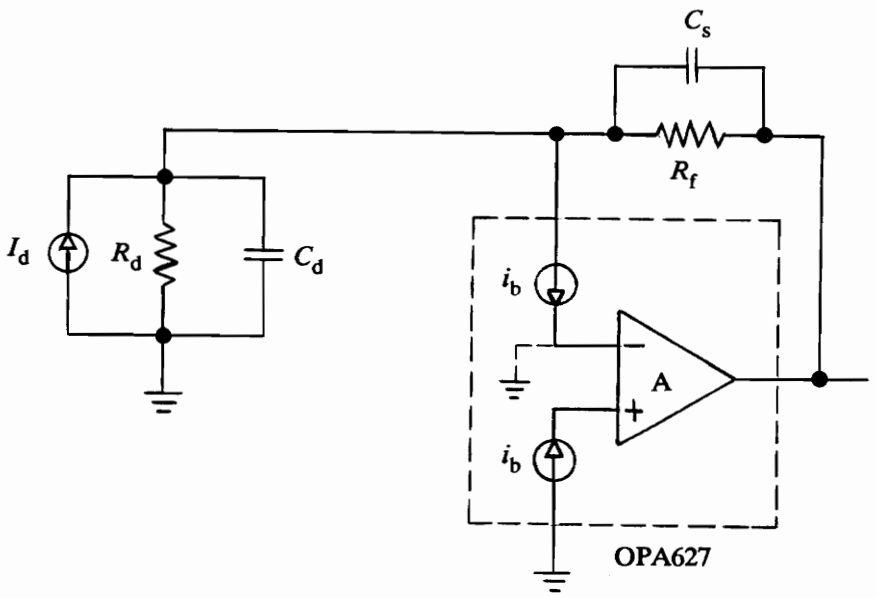

A. "Noiseless" amplifier

Figure 33 Equivalent noise circuit for the primary stage of the prototype DAV's circuitry

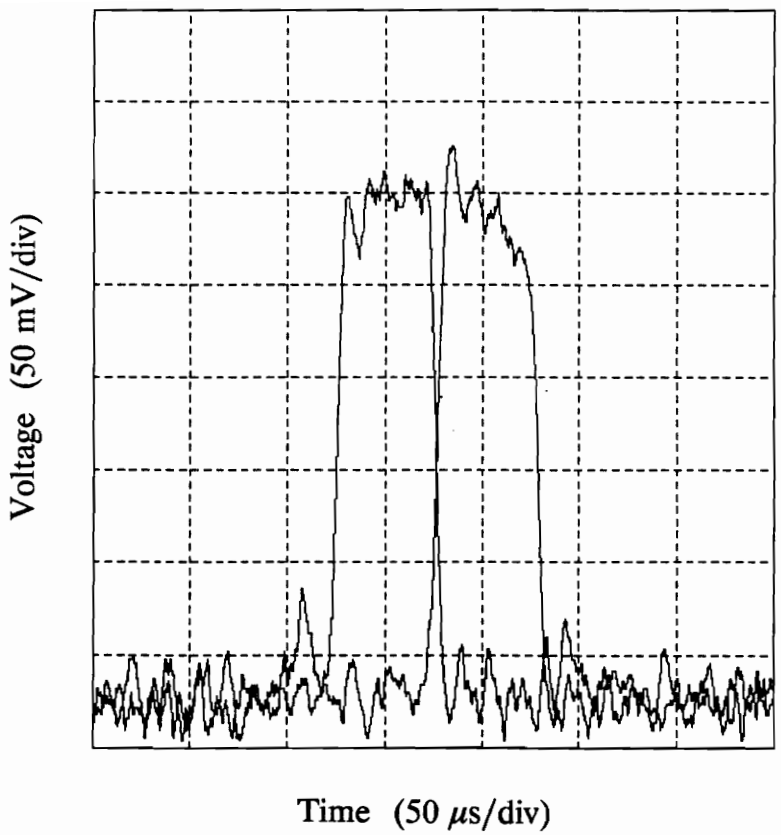

Figure 34 Various voltage signals produced by the prototype DAV while measuring a seeded flow with a freestream velocity of 10 m/s: (a) example signal pair

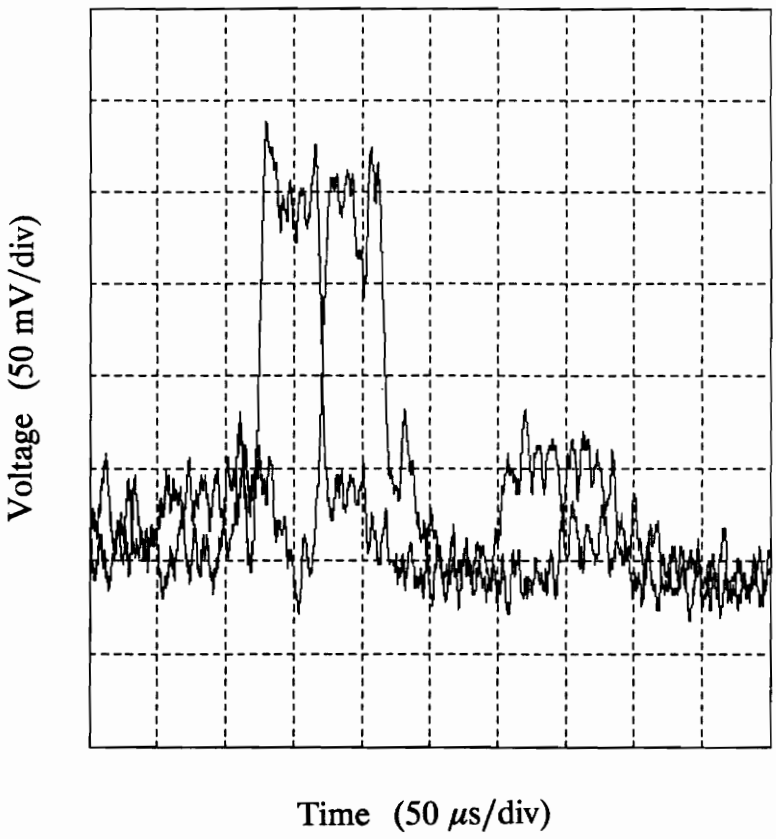

Figure 34 (continued) (b) 'good' quality signal pair

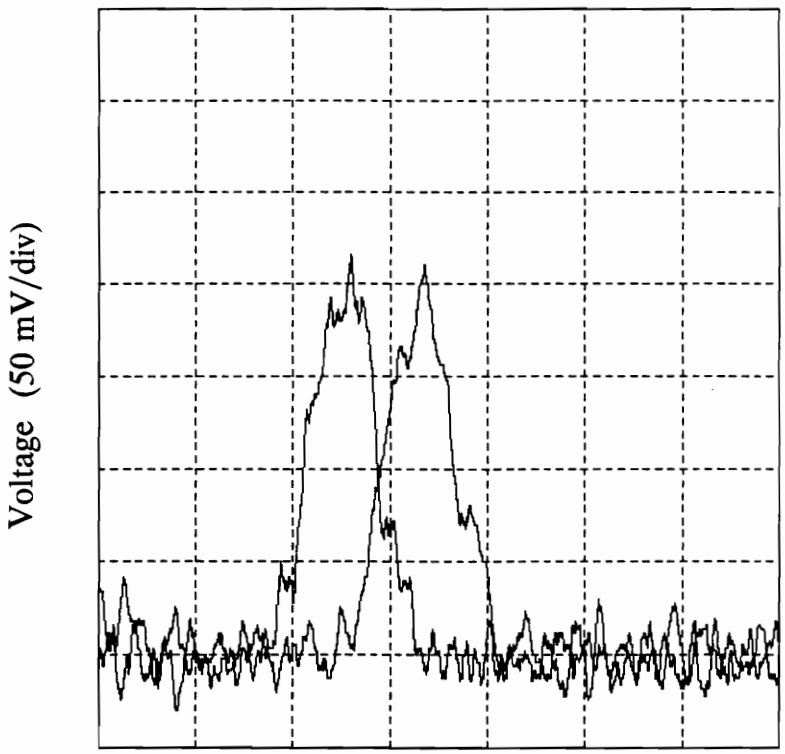

Figure 34 (continued) (c) 'poor' quality signal pair

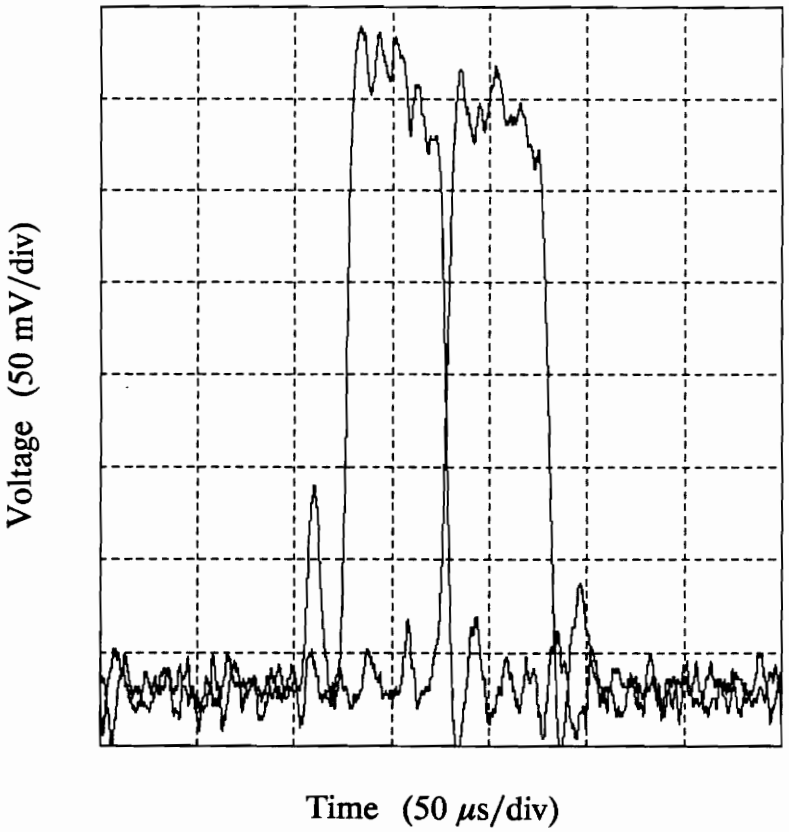

Figure 34 (continued) (d) signal pair with large spikes riding on them

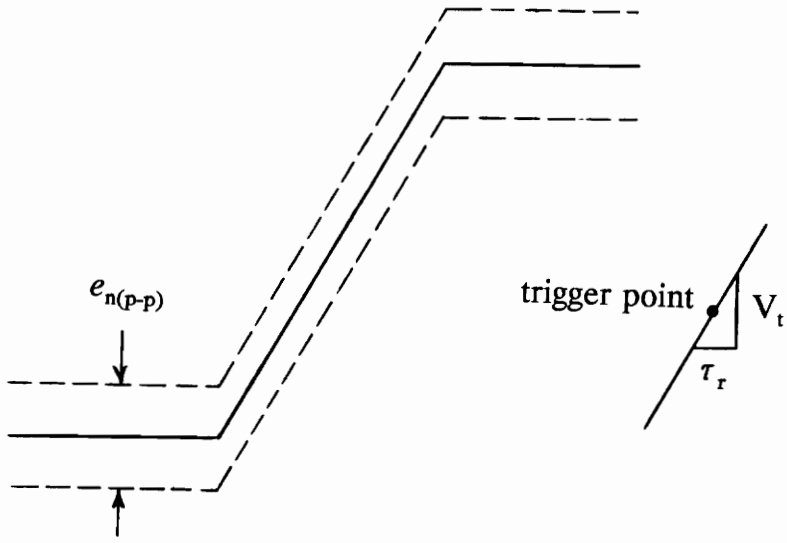

Figure 35 Leading edge of an idealized voltage signal with peak-to-peak noise bands shown

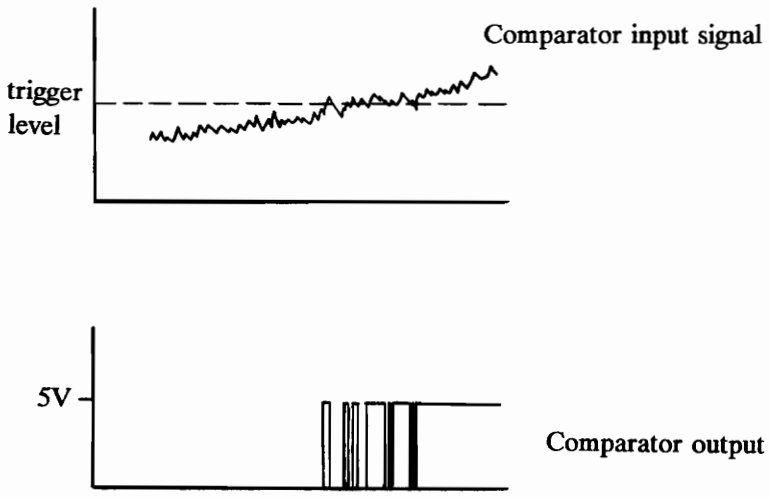

Figure 36 A noisy voltage signal crossing its trigger level causes the comparator amplifier's output to switch states many times (multiple triggering)

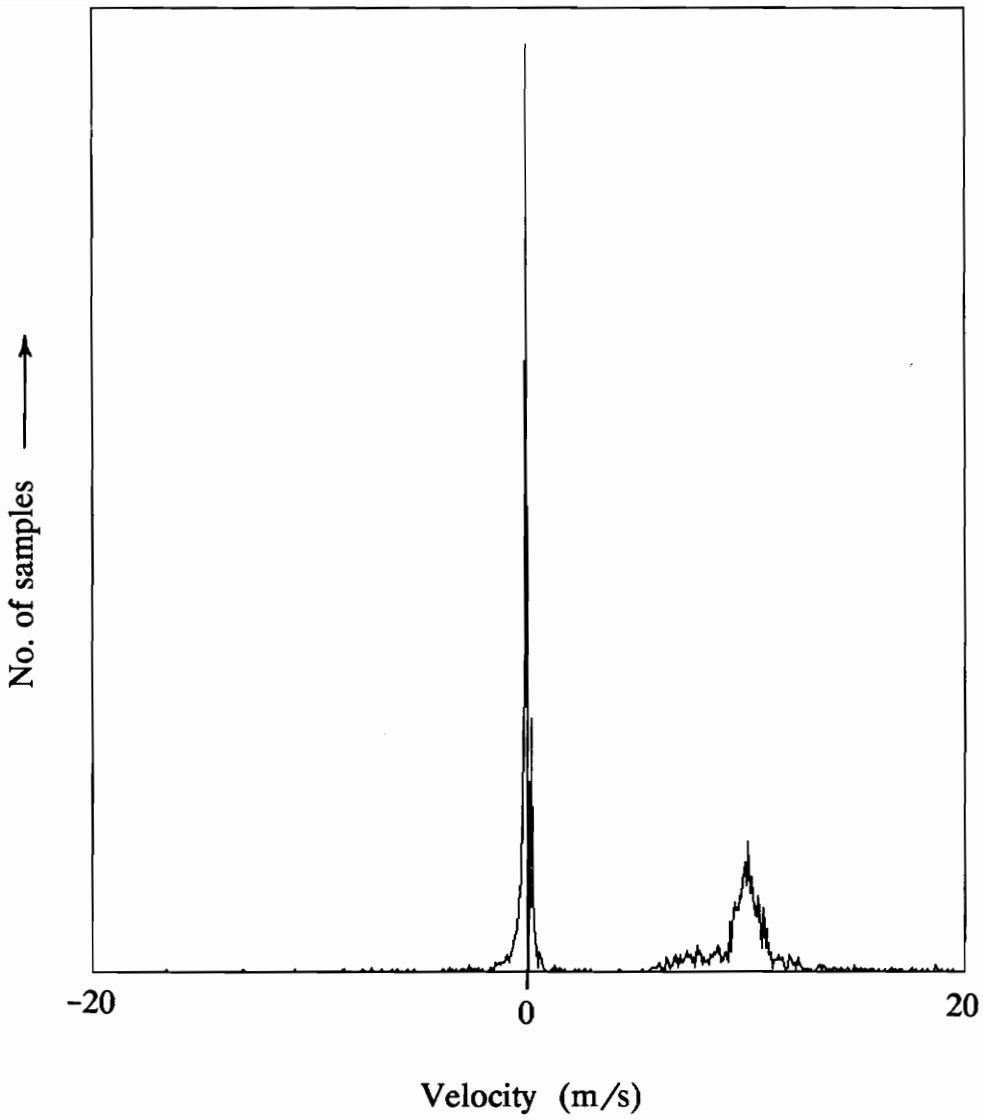

Figure 37 Velocity histogram showing the error due to trigger misfires; graph contains approximately 1000 samples

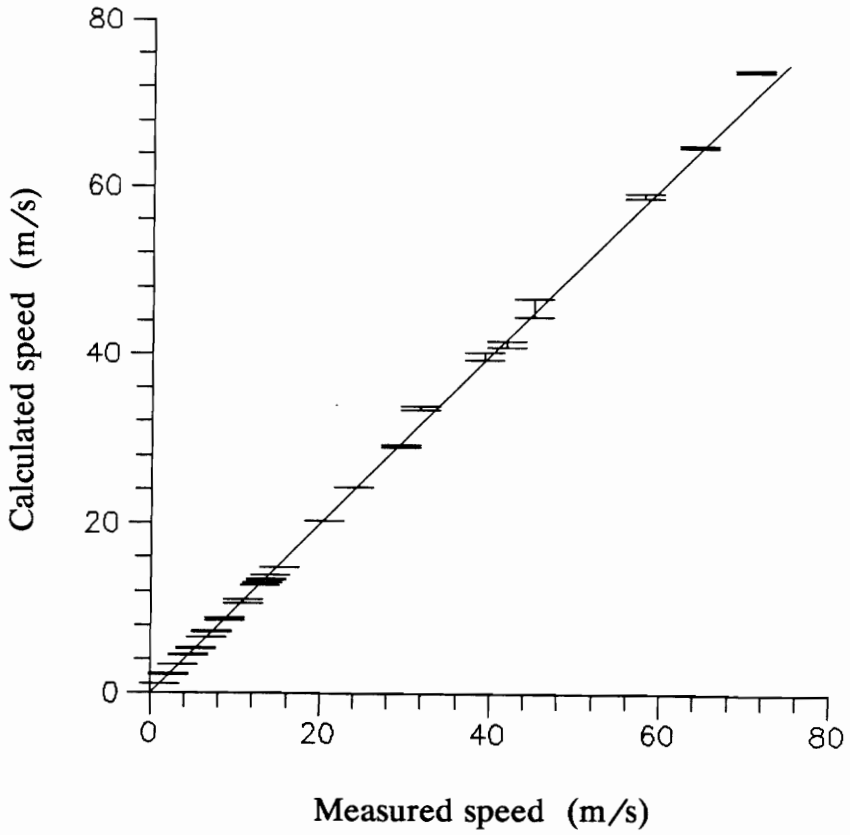

Figure 38 Rotating disk speed measured by the prototype DAV vs. speed calculated by a semi-independent method; solid line has a slope of 1

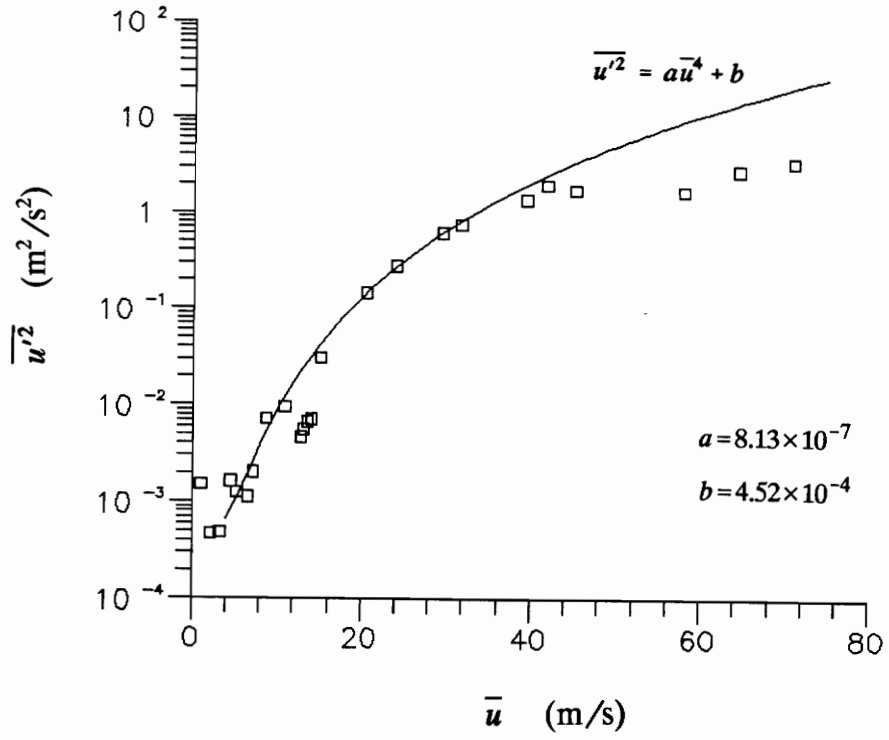

Figure 39 Rotating wire's turbulence stress measured with the prototype DAV vs. wire's mean velocity; solid line shows theoretical curve

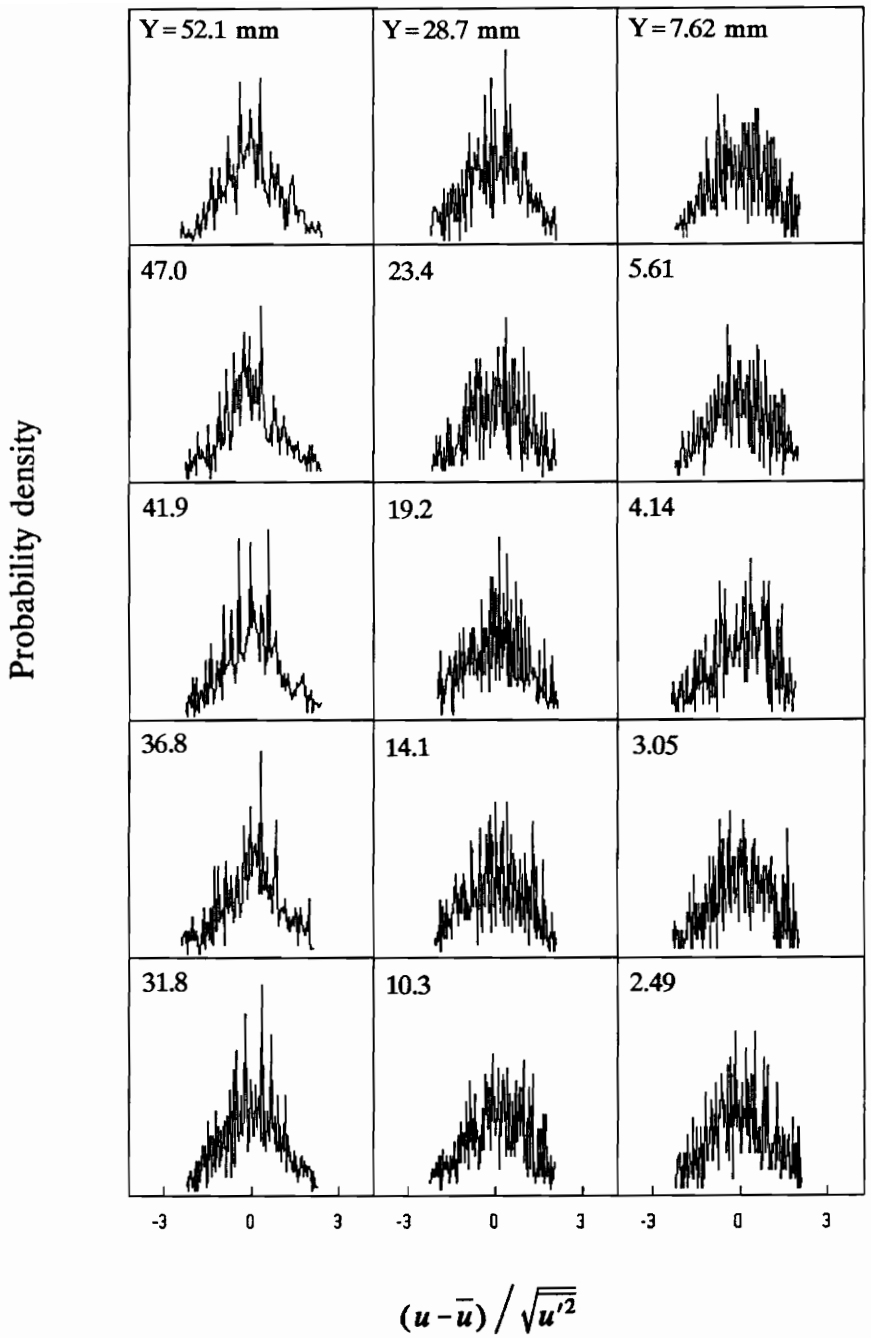

Figure 40 Velocity probability distributions of the prototype DAV's profile data; Y location of measurement is shown in upper left hand corner of each graph

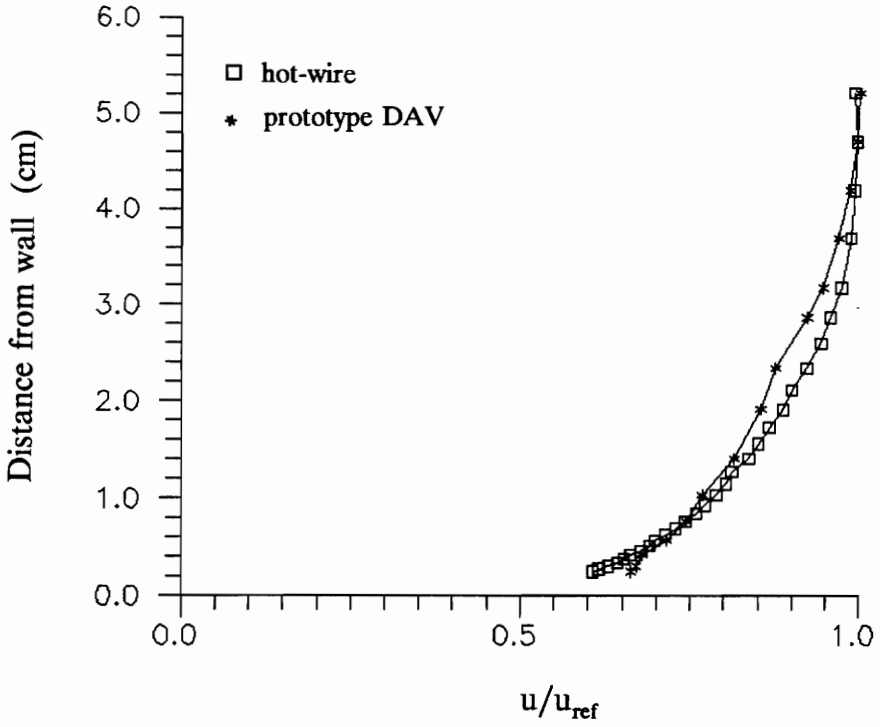

Figure 41 Mean velocity data taken by the prototype DAV and a hot-wire anemometer in a turbulent wall bounded flow with a freestream velocity of 10 m/s

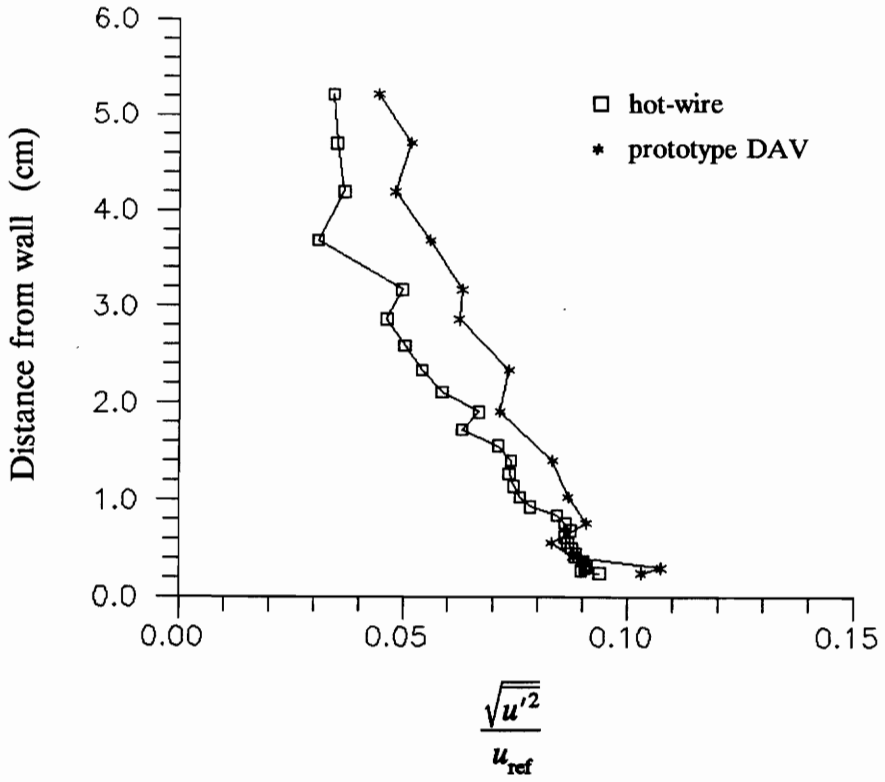

Figure 42 Turbulence intensity data taken by the prototype DAV and a hot-wire anemometer in a turbulent wall bounded flow with a freestream velocity of 10 m/s

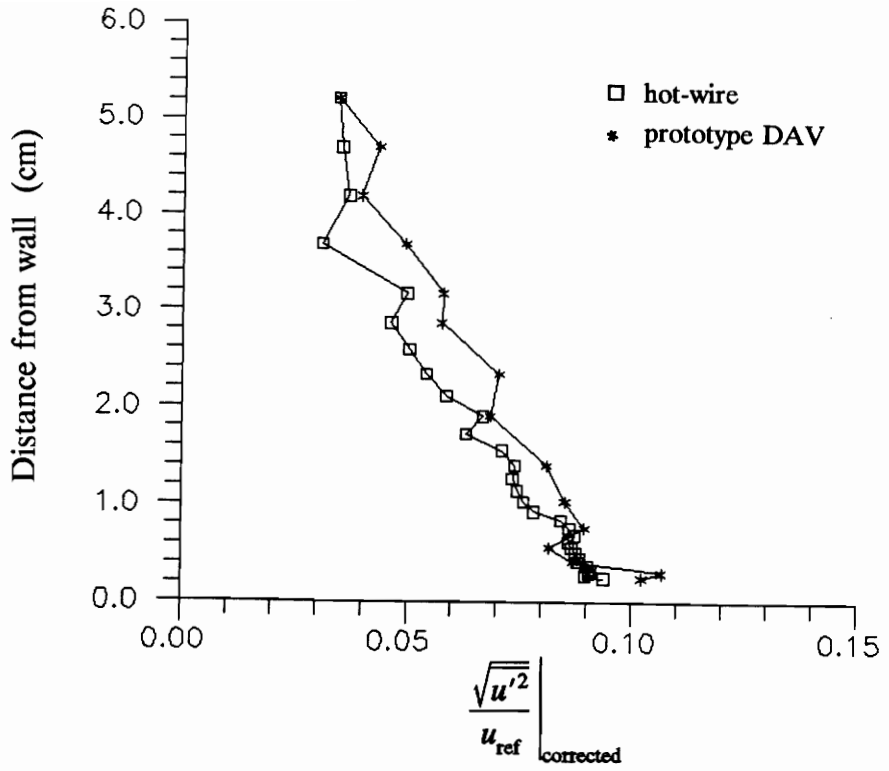

Figure 43 Turbulence intensity measured by the hot-wire plotted with turbulence intensity measured by the prototype DAV after correcting for the prototype's estimated error

Vita

The author was born on September 10, 1967, in Berkeley, California. He was raised in Fairfax, Virginia, by his parents Edward and Jane Smith. After attending W. T. Woodson High School he enrolled at Virginia Polytechnic Institute & State University in the fall of 1985. He received his B.S. degree in Aerospace Engineering in December of 1989, and then stayed on to pursue a master's degree in the same field.